Realistic Total-Body J-PET Geometry Optimization - Monte Carlo Study

Jakub Baran, Wojciech Krzemien, Lech Raczyński, Mateusz Bała, Aurelien Coussat, Szymon Parzych, Neha Chug, Eryk Czerwiński, Catalina Oana Curceanu, Meysam Dadgar, Kamil Dulski, Kavya Eliyan, Jan Gajewski, Aleksander Gajos, Beatrix Hiesmayr, Krzysztof Kacprzak, Łukasz Kapłon, Konrad Klimaszewski, Grzegorz Korcyl, Tomasz Kozik, Deepak Kumar, Szymon Niedźwiecki, Dominik Panek, Elena Perez del Rio, Antoni Ruciński, Sushil Sharma, Shivani, Roman Y. Shopa, Magdalena Skurzok, Ewa Stępień, Faranak Tayefiardebili, Keyvan Tayefiardebili, Wojciech Wiślicki, Paweł Moskal

***Abstract*— Total-Body PET imaging is one of the most promising newly introduced modalities in the medical diagnostics. State-of-the-art PET scanners use inorganic scintillators such as L(Y)SO or BGO, however, those technologies are very expensive, prohibitng the broad total-body PET applications. We present the comparative studies of performance characteristics of the cost-effective Total-Body PET scanners using Jagiellonian PET (J-PET) technology that is based on plastic scintillators. Here, we investigated *in silico* five realistic Total-Body scanner geometries, varying the number of rings, scanner radius, and distance between the neighbouring rings. Monte Carlo simulations of two NEMA phantoms (2-meter sensitivity line source and image quality) and the anthropomorphic XCAT phantom, were used to assess the performance of the tested geometries. We compared the sensitivity profiles and we performed the quantitative analysis of the reconstructed images by using the quality metrics such as contrast recovery coefficient, background variability and root mean squared error. The optimal scanner design was selected for the first Total-Body J-PET scanner configuration.**

***Index Terms*— J-PET, Total-Body PET, Monte Carlo, TOF PET, medical imaging, molecular imaging**

The authors gratefully acknowledge the support of the Foundation for Polish Science through programme TEAM POIR.04.04.00-00-4204/17; the National Science Centre of Poland through grant nos. 2019/35/B/ST2/03562, 2020/38/E/ST2/00112, 2021/42/A/ST2/00423 and 2021/43/B/ST2/02150; the Ministry of Education and Science under the grant No. SPUB/SP/530054/2022; EU Horizon 2020 research and innovation programme, STRONG-2020 project, under grant agreement No 824093; the Jagiellonian University via the project CRP/0641.221.2020, and via SciMat and qLife Priority Research Areas under the program Excellence Initiative-Research University at the Jagiellonian University.

J. Baran, A. Coussat, S. Parzych, N. Chug, E. Czerwiński, M. Dadgar, K. Dulski, K. Eliyan, A. Gajos, K. Kacprzak, Ł. Kapłon, G. Korcyl, T, Kozik, D. Kumar, S. Niedźwiecki, D. Panek, E. Perez del Rio, S. Sharma, Shivani, M. Skurzok, E. Stępień, F. Tayefiardebili, K. Tayefiardebili, P. Moskal are with the Faculty of Physics, Astronomy and Applied Computer Science, Jagiellonian University, Kraków, Poland, Total-Body Jagiellonian-PET Laboratory, Jagiellonian University, Kraków, Poland and Center for Theranostics, Jagiellonian University, Kraków, Poland (e-mails: jakubbaran92@gmail.com aurelien.coussat@uj.edu.pl, szymon.parzych@doctoral.uj.edu.pl, neha.chug@doctoral.uj.edu.pl, eryk.czerwinski@uj.edu.pl, meysam.dadgar@doctoral.uj.edu.pl, kamil.dulski@gmail.com, kavyavalsane@gmail.com, aleksander.gajos@uj.edu.pl, k.kacprzak@alumni.uj.edu.pl, lukasz.kaplon@uj.edu.pl, grzegorz.korcyl@uj.edu.pl, ufkozik@cyf-kr.edu.pl, deepak.kumar2014@gmail.com, szymon.niedzwiecki@uj.edu.pl, dominik.panek@doctoral.uj.edu.pl, elena.rio@uj.edu.pl, sushil.sharma@uj.edu.pl, shivani.shivani@doctoral.uj.edu.pl, magdalena.skurzok@uj.edu.pl, e.stepien@uj.edu.pl, faranak.tayefiardebili@gmail.com, keyvan.tayefiardebili@doctoral.uj.edu.pl, ufmoskal@if.uj.edu.pl).

W. Krzemien is with High Energy Physics Division, National Centre for Nuclear Research, Otwock-Świerk, Poland and with Total-Body Jagiellonian-PET Laboratory, Jagiellonian University, Kraków, Poland, Center for Theranostics, Jagiellonian University, Kraków, Poland and (e-mail: wojciech.krzemien@ncbj.gov.pl).

M. Bała, L. Raczyński, K. Klimaszewski, R. Y. Shopa, W. Wiślicki are with the Department of Complex Systems, National Centre for Nuclear Research, Otwock-Świerk, Poland (e-mails: bala.mateusz@gmail.com, lech.raczynski@ncbj.gov.pl, konrad.klimaszewski@ncbj.gov.pl, roman.shopa@ncbj.gov.pl, wojciech.wislicki@ncbj.gov.pl).

C. Curceanu is with INFN, Laboratori Nazionali di Frascati, Frascati, Italy (e-mail: catalina.curceanu@lnf.infn.it).

J. Gajewski, A. Ruciński are with Institute of Nuclear Physics, Polish Academy of Sciences, Kraków, Poland (e-mails: jan.gajewski@ifj.edu.pl, antoni.rucinski@ifj.edu.pl).

B.C. Hiesmayr is with Faculty of Physics, University of Vienna, Vienna, Austria (e-mail: beatrix.hiesmayr@univie.ac.at).

I. Introduction

Positron emission tomography (PET) is a state-of-the-art diagnostic technique enabling metabolic imaging of the pathological tissues [1]–[4]. Nowadays, routine PET machines offer about 20-25 cm axial Field-Of-View (FOV) with a single bed position. In order to perform an image of the whole patient's body, a series of scans obtained with different bed positions are needed. The new generation of Total-Body (TB) PET scanners [5]–[9] enables simultaneous imaging of the whole human body, which opens new perspectives in dynamic imaging, kinetic modelling [10]–[15], and positronium imaging [16]–[18].

The inorganic L(Y)SO scintillators are the most popular choice, which results in very high costs of the existing TB scanners, estimated to be in the range of about $10 million or more [19]. This price is unaffordable for most hospitals and research facilities which makes the technology hard to implement in clinical routine. To reduce the TB scanner cost, various approaches have been proposed, including reduction of the scintillator thickness [20], [21], rearranging the scintillators to the sparse configurations [22], [23], use of the BGO crystals to improve the timing information with the Cherenkov lightning [24]–[27] or use of plastic scintillators [28], [29]. It

is also worth mentioning that projects aiming to combine PET imaging with Compton cameras are ongoing [30]–[38].

A cost-effective, portable and modular PET scanner (J-PET) with an extended 50-cm long AFOV is under commissioning at the Jagiellonian University in Kraków. The scanner is built based on EJ-230 (ELJEN Technology) plastic scintillator strips. In the J-PET, annihilation photons interact with the scintillator strips via Compton scattering. Deposited energy is converted into scintillation light which is then collected at the ends of the scintillators by the silicon photomultipliers (SiPM) and read out by fast, customized on-board front-end electronics enabling time-of-flight (TOF) measurement [39]. The J-PET scanner application is not limited only to the standard medical two-photon imaging [29], but it provides the possibility to perform multi-gamma tomography e.g. positronium imaging [16], [40]. Furthermore, it is utilized for fundamental physics studies on quantum entanglement [41], studies of discrete symmetries in nature [40], proton beam range monitoring in hadron radiotherapy [38], [42], [43], and PET data reconstruction methods development [44], [45]. Currently, works toward the 200-cm axial FOV Total-Body J-PET scanner (TB J-PET) are ongoing [29], [46].

The main aim of this work is to investigate and compare the characteristics of five realistic geometry options for the design of the new TB J-PET device.

Our previous studies focused on the J-PET scanner performance for idealized geometries. The first investigation [28] considered scanners with axial FOV up to 100 cm. The next studies [29] were dedicated to 140 cm and 200 cm long prototypes. In all cases, the scanner model consisted of long plastic strips tightly arranged in a cylinder. In the early article [28] scanner-based characteristics were determined such as sensitivity, spatial resolution, scatter fraction (SF) and noise equivalent count rate (NECR). For the latter publication [29], the image quality metrics for the NEMA IEC phantom were estimated for the 140 cm long axial FOV scanner.

In this study, a different approach has been undertaken. To make the simulation conditions more realistic, we take into account the size of the front-end electronics, and the gaps between adjacent rings, as well as inactive detector material. Additionally, the length of the scintillator strips is restricted to 686.4 mm and 330.0 mm, to improve light yield in the scintillator which is strongly attenuated in longer strips [47]. In consequence, longer scanners are constructed by combining adjacent rings of cylindrical strips. Beyond sensitivity, SF and NECR, we assess the quality of the reconstructed images simulating the NEMA IEC and extended cardiac-torso phantoms (XCAT). Also, we expand the previously used metrics such as contrast recovery coefficient (CRC) and background variability (BV), by adding the Root Mean Square Error (RMSE), and the Q metric which combines the CRC and BV.

Based on the performed analysis, the first TB J-PET scanner configuration is selected.

II. Materials and Methods

A. Monte Carlo simulation parameters

J-PET scanner geometries were modeled using GATE v9.0 [48], [49], based on Geant v4.10.7.1 [50]. An additional layer of Wave Length Shifters (WLS), which improves the estimation of the axial coordinate of the photon interaction point [47], was incorporated into the simulation model. The default GATE digitizer code was extended to allow the simulation of the signals registered in the WLS layers. In all the simulations the em_livermore_polar physics list was used, which is the standard choice for all J-PET-related MC simulations [29]. The tracking of optical photons was not included in the simulations to reduce the computation time. In all the simulations, the β^+ source decay is not simulated directly and simulation starts at the emission of the back-to-back photon pairs. The direction of the emission is randomized isotropically. The energy of the initial photons is set to 511 keV.

B. Phantoms

We simulated the NEMA sensitivity, NEMA Image Quality (NEMA IEC) [51] and XCAT [52] phantoms [29].

The NEMA sensitivity phantom consists of the 2-meter linear source positioned in the center, along the long axis of the cylindrical scanner. For each simulation, the activity of 10^7 Bq and measurement time of 1000 seconds were used.

22 cm long NEMA IEC phantom is built out of four high-activity (denoted as *hot*) and two low-activity (denoted as *cold*) spheres. The phantom was positioned isocentrically within the scanners. Hot spheres of 10 mm (Sphere 10), 13 mm (Sphere 13), 17 mm (Sphere 17) and 22 mm (Sphere 22) diameters and cold spheres of 28 cm and 37 mm diameters were simulated. The ratio between the hot spheres and the background was set to 4:1. The total activity of 59 MBq was simulated and the acquisition time was set to 500 seconds. The NEMA IEC phantom activity map is depicted in Fig. 1.

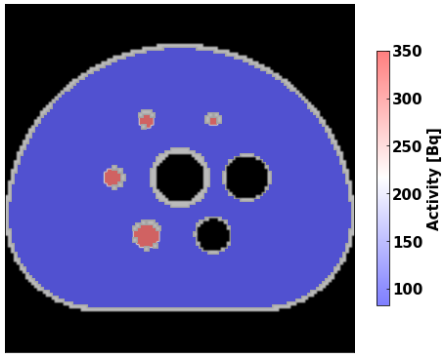

Fig. 1. Activity distribution of the NEMA IEC phantom. The activity map was superimposed on the CT image.

The activity of the male XCAT phantom [52] was prepared [53], [54] to mimic the ^{18}F-FDG distribution within the human body. Additionally, two hot spheres (diameter = 1.2 cm) positioned in the lung and in the liver were incorporated in the phantom simulations. The contrast between the hot region and the background activity was set to 16:1 and 3:1 for lungs and liver, respectively. The overall activity of the phantom was equal to 50 MBq and the acquisition time was set to 600 seconds. The XCAT phantom activity map is depicted in Fig. 2.

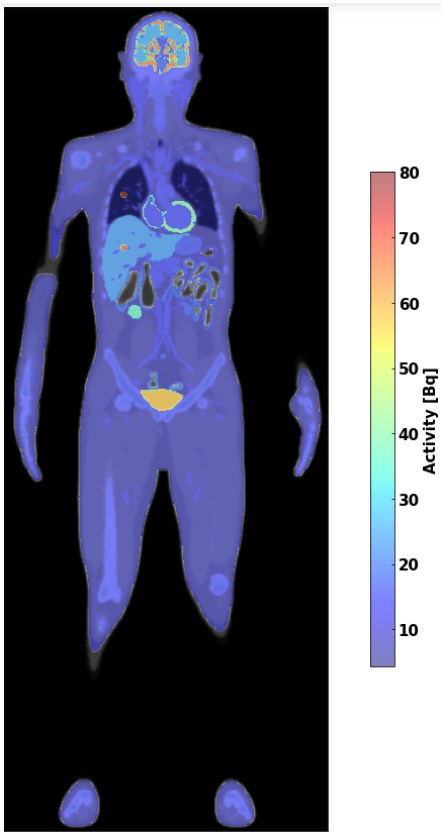

Fig. 2. Activity distribution of the XCAT phantom superimposed on the CT image. Two hot spots (red color) representing the activity lesions originating from cancerous centers in the liver and lung are shown.

C. Total-Body J-PET scanner geometries

Five two-layer TB J-PET scanner configurations were studied. Scanners with varying numbers of rings, length of the gap between the subsequent rings, scanner radius, and scintillators cross-sections were investigated. All scanner models consist of cylindrically arranged strips of plastic scintillators in two layers. 32 plastic scintillator strips (16 strips per layer) were grouped into modules. Each ring consists of 24 modules arranged cylindrically. Depending on the scanner setup, three (S1, S2, S3) or seven (S4, S5) rings positioned axially next to each other were considered with lengths of 686.4 mm and 330.0 mm, respectively. Additionally, two gap length values between adjacent rings were simulated: 2 cm (S1, S3, S4, S5) and 5 cm (S2). Scanner setups were also differentiated in scintillator cross-section: 25 x 5.7 mm^2 (S1, S2, S3), 25 x 6.0mm^2 (S4), 30 x 6.0mm^2 (S5). The positioning of the strips inside the module is depicted in Fig. 3. The chemical composition of the scintillator corresponds to the commercial EJ230 scintillator, which is used in the existing J-PET scanner prototypes [16], [29]. The summary of the scanner properties is given in Table I and the visualisation of the S5 modality is shown in Fig. 4.

In all cases, the modules were placed as close as possible on a radius. The difference in radius between S1-S3 and S4-S5 results from that for S1 and S2 the electronics were constructed to be larger the module cross section which caused a significantly greater radius with respect to the S3-S5. In both cases, the scintillator cross section is set to fit the size of SIPMs active surface equal to 6×6 mm^2.

The selection of these scanner geometries allows for studying the impact of several parameters (see Tab. I) on the system performance. Scanners S1 and S2 give insight into the influence of the gap between the rings. The 2 cm gap corresponds to the smallest mechanically possible distance, where all the front-end electronics components are tightly packed, while 5 cm space allows for some flexibility in the mechanical construction. The difference between S1 and S3 modality lays mainly in the two radius values. The use of the smaller radius permits decreasing the number of readout channels. The S4 and S5 scanners are used to study the effect of the scintillator width on sensitivity. Finally, the S3 and S4 modality use different scintillator lengths since the smaller the length the better the timing resolution [28], [29].

TABLE I
SCANNERS PROPERTIES

Property	Scanner geometry				
	S1	*S2*	*S3*	*S4*	*S5*
Radius [mm]	506	506	425	414.65	414.65
Axial FOV [mm]	2099.2	2159.2	2099.2	2430	2430
Scintillator length [mm]	686.4	686.4	686.4	330	330
Scintillator cross-section [mm]	25x5.7	25x5.7	25x5.7	25x6.0	30x6.0
No of adjacent rings	3	3	3	7	7
Gap between adjacent rings [mm]	20	50	20	20	20

D. Photon detection, coincidence formation and energy threshold

The front-end electronic response was modelled by the GATE digitizer which converts photon interaction in the scintillator into deposited energy and detection time.

The temporal and energetic resolution of the detection system was taken into account in the simulation by the phenomenological parameterisation of the experimental resolutions. The energy resolution dependence is parameterised as a $\frac{\sigma(E)}{E}$ fraction which reflects the experimentally determined relation for the plastic scintillator strips [55]:

$$\frac{\sigma(E)}{E} = \frac{0.044}{\sqrt{E(MeV)}} \quad (1)$$

.

The simulated photon registration time is smeared, event by event, by replacing the event registration time t_r by the value obtained from the normal distribution $N(t_r, \sigma_t)$, where σ_t corresponds to the temporal resolution of the scintillator strip. Analogically, the registration position along the scintillator strip (z position) is smeared, event by event, by replacing the registered photon position z by the value obtained from the normal distribution $N(z, \sigma_z)$, where σ_z corresponds to the positional uncertainty along the scintillator strip of the scanner. For all the simulations the resolution parameters, i.e., the position along the strip and the time were set to σ_z equal to

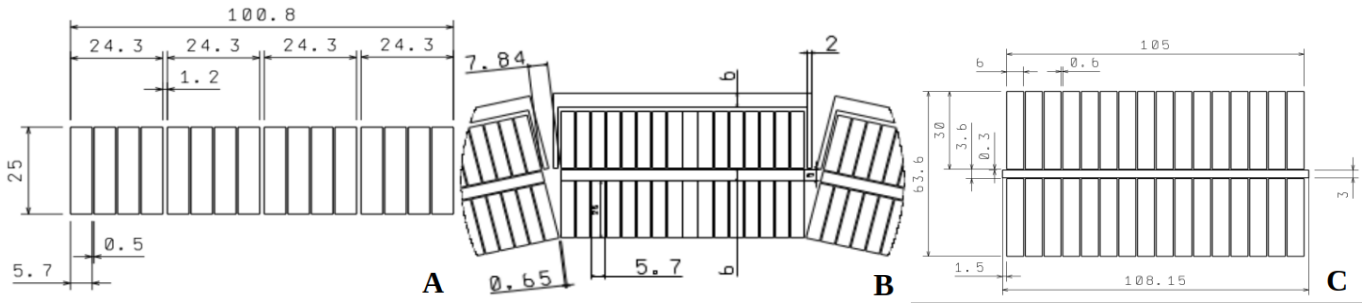

Fig. 3. Schematic drawings of the modules cross-sections for S1 and S2 (panel A), S3 (panel B) and S5 (panel C). Due to the complexity of the module for S1 and S2 only one layer is depicted. For the S3, the dimension of the scintillator in radial direction (width) is equal to 25 mm. The distance between layers is equal to 6 mm for scanners S1, S2 and S3. S4 is not shown, but the only difference between the modules for S4 and S5 is the width of the plastic scintillator which is equal to 25 mm and 30 mm, respectively. WLS layer is placed between scintillator layers and is only considered for the scanners S4 and S5. The gap between neighbouring plastic strips for scanner S3 (panel B) is equal to 1 mm. All the dimensions are given in mm.

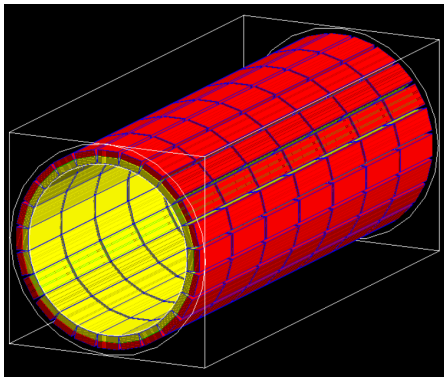

Fig. 4. Visualisation of the 7-ring S5 scanner. The length of the scintillators in each ring is equal to 33 cm. The gap between adjacent rings is equal to 2 cm. It results in 243 cm axial FOV. Two layers of the scanners are shown (yellow and red strips).

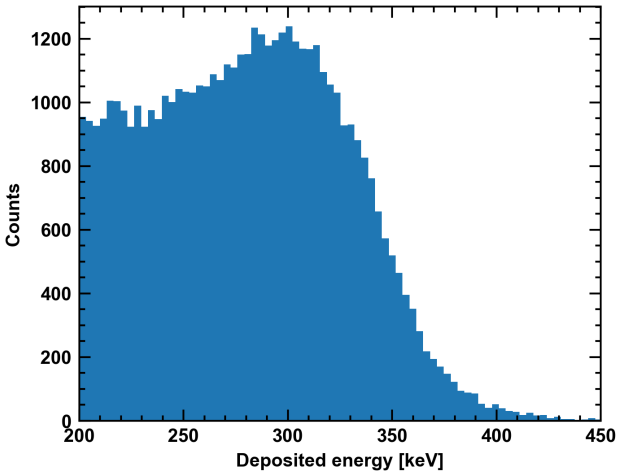

Fig. 5. Deposited energy distribution in the plastic scintillator obtained from the Monte Carlo simulations. The Compton edge is smeared due to the energy resolution model included in the simulations. The photons which deposit the energy below the threshold of 200 keV are rejected.

2.12 mm [29] and σ_t equal to 100 ps (scanners S1, S2 and S3) or 77 ps (scanners S4 and S5), respectively. Discrepancies in time smoothing reflect the expected time resolution change due to the size of the scintillator strip length [29], [56], [57]. The coincidence time window of 3 ns was used. In contrast to the inorganic detectors, in plastic scintillators the photons deposit their energy mainly via Compton scattering. The additional energy selection threshold E_{thr} of 200 keV was set to reduce the fraction of the background coincidence events, for which at least one of them undergoes the scattering in the phantom before being registered in the scanner. Only coincidence pairs with the registration photon energy above the energy threshold are considered. This selection criterion corresponds to the optimal selection cut applied in analysis of the data obtained with the J-PET prototype allowing for the reduction of scattering in the patient and in the detectors [28], [29], [55]. The exemplary distribution of the deposited energy in the plastic scintillator is shown in the Fig. 5.

E. Data preselection and preparation

For the image reconstruction analysis, only genuine, true coincidences were taken into account. In addition, for all the simulations, the numbers of true, scatter and random coincidences were determined, and, the scatter fraction (SF) was calculated as:

$$SF = \frac{N_{scatter}}{N_{true} + N_{scatter}}, \tag{2}$$

where $N_{scatter}$ and N_{true} are the numbers of true and scatter coincidences, respectively.

Moreover, the noise equivalent count rate (NECR) was calculated as:

$$NECR = \frac{T^2}{T + S + R}, \tag{3}$$

where T, S and R are the true, scatter and random coincidences rates given in kcps.

For the image quality metrics calculation the background and contrast region-of-interests (ROIs) were defined as described by the NEMA norms [51]. For the XCAT phantom analysis instead of 2-dimensional areas, 3D ROIs were used. ROIs for the quantitative analysis do not included the whole hot region but were morphologically eroded to overcome the partial volume effects. 15 background ROIs were chosen

separately for the liver and lungs regions. Both, hot sphere and background ROIs, are composed of 52 voxels. To avoid the partial volume effect, an additional constraint, that the background ROI cannot be neighbouring the region of different activities, was applied [58]. The exemplary positioning of the ROIs is shown in Fig. 6.

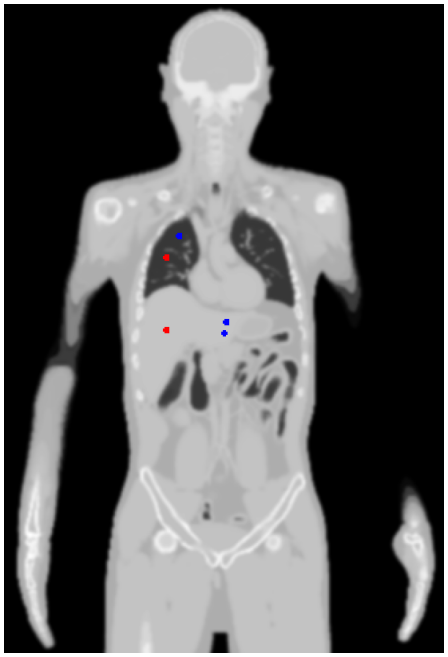

Fig. 6. Positioning of the exemplary hot (red circle) and background (blue circle) ROIs used for the image quality assessment. ROIs are superimposed on the CT image used for the simulations. In total, 1 hot and 15 background ROIs were prepared for the liver and lungs separately.

F. PET image reconstruction

The image reconstruction was performed with the CASToR software package [59]. TOF List Mode - Maximum Likelihood Expectation Maximization algorithm with 50 iterations were used. TOF resolution kernel was modelled as the Gaussian function. Sensitivity and attenuation corrections were included. The multi-Siddon projector with 10 rays was used. Reconstructed images were smoothed with 3D Gaussian post-filter with σ set to 2.5 mm. No additional resolution modelling was used in the reconstruction process.

G. TOF resolution optimization

The CASToR software provides the possibility to use the shift-invariant TOF kernel only. This approach can be sub-optimal, especially while dealing with the large FOV scanners, where the kernel shape can change significantly in the axial direction [60]. However, the main aim of these studies is the relative comparison between the performance of scanner configurations, and the usage of the shift-invariant TOF kernel affects all the investigated setups in a rather equal manner.

On the other hand, it is expected that the optimal width of the shift-invariant Gaussian kernel should be larger than the one determined by the nominal TOF resolution, because of the additional uncertainty of the hit registration position along the axial direction of the strip that effectively smears the overall TOF resolution (see Fig. 7). Therefore, we performed an investigation to choose the optimal shift-invariant Gaussian kernel width, which was used in further studies.

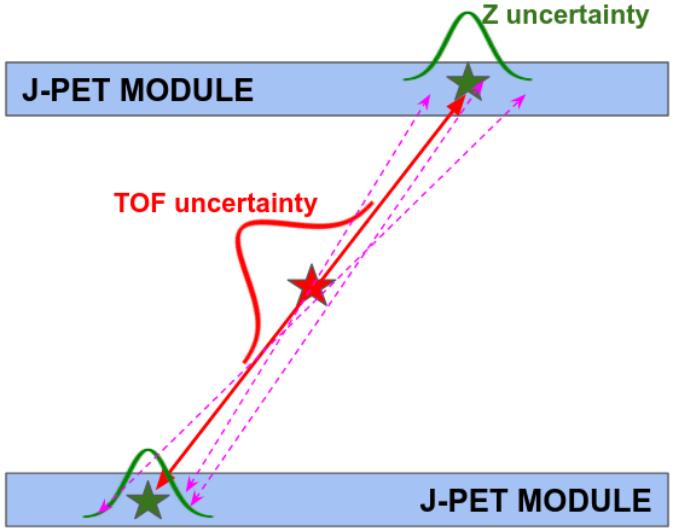

Fig. 7. The picture presents the TOF uncertainty phenomena for the J-PET. Apart from the well-known TOF uncertainty along the line of response (red color) additional effect of the uncertainty of the hit registration along the plastic scintillator (green color) needs to be addressed in the case of the J-PET technology. It results in larger shift-variant Gaussian kernel than the one determined by the nominal TOF. Exemplary modelled line of responses are shown in violet.

Five different Full Width Half Maximum (FWHM) kernel values: 115 ps, 230 ps, 365 ps, 500 ps and 750 ps were selected. The investigation was performed with both NEMA IEC and XCAT phantoms.

H. System sensitivity and image quality metrics

The performance of the scanners has been evaluated based on several criteria including the sensitivity profiles, SF, NECR and image quality metrics.

The sensitivity of the scanner S is defined as the rate of detected genuine coincidences (counts per second) per unit of the radioactivity concentration. In the first order, the sensitivity is proportional to the geometrical acceptance of the scanner (A), detection efficiency of the photon pair ϵ^2 and the fraction of events f accepted after applying the energy window. For the point source placed in the scanner center we define theoretical sensitivity as follows:

$$S_{theor}(L,R) = A(L,R) \times \epsilon^2 \times f, \tag{4}$$

where L and R are axial field-of-view and radius of the scanner, respectively.

For the cylindrical scanner the geometric acceptance can be approximated as:

$$A(L,R) = \frac{1}{2} \times k \times \frac{L}{\sqrt{\frac{L^2}{4} + R^2}}, \tag{5}$$

where the k factor accounts for the holes and inactive detector components.

The evaluation of the reconstruction performance is based on the metrics defined in the NEMA NU 2–2018 norm for image quality assessment [51]. The procedure is to choose two types of ROIs within the reconstructed image and determine their statistical properties. The first ROI corresponds to the expected high activity (*hot*) signal region and the second ROI corresponds to low activity background region(s) ROI. The *CRC* for a given region of interest is defined as:

$$CRC = \frac{C_S - C_B}{C_B} : \frac{a_S - a_B}{a_B}, \tag{6}$$

where C_S, C_B is the average number of counts determined for signal and background ROI, and a_S, a_B are the signal and background activities, respectively.

The *BV* is defined as a standard deviation (S_B) calculated for the background ROI normalized to the average counts in the background region:

$$BV = \frac{S_B}{C_B}. \tag{7}$$

We inspected the additional metric Q, which combines the information from both, CRC and BV, and is defined as [44]:

$$Q = |CRC - 1| + BV. \tag{8}$$

The Q value range is given by: $Q \in [0, \infty)$. For the perfect image reconstruction in terms of CRC and BV, one expects 1 and 0 for CRC and BV, respectively. By definition, Q would also be equal to 0.

In addition, Root Mean Squared Error (RMSE) metric was used to assess the image quality. The RMSE between two images I_1 and I_2 is defined as:

$$RMSE[I_1, I_2] = \frac{1}{N}\sqrt{\sum_{k=1}^{N}(I_1[k] - I_2[k]))^2}, \tag{9}$$

where the N is the total number of voxels, respectively.

In our studies, the activity emission map was used as a ground-truth reference image. Prior to the $RMSE$ calculation, the compared reference and reconstructed images were first normalized to the maximum. Then, the median intensities were calculated for both. For NEMA IEC and XCAT phantom, whole phantom and body areas were used to calculate medians. Subsequently, the ratio between medians was calculated and finally, the reconstructed image was scaled by the ratio.

III. Results

A. Sensitivity

Sensitivity plots for the simulated scanners are shown in Fig. 8. Analytical and Monte Carlo-based sensitivity in peak values are given in Table II. Results of peak values based on Monte Carlo simulations are in a good agreement with the theoretical calculations. The underestimation of the analytical calculations compared to the Monte Carlo is a result of not considering the depth of the crystal in the calculation of the k factor from Eq. 5. The greatest sensitivity has been found for the scanner S5 with the maximum at the level of 34 cps/kBq. The lowest value is observed for the scanner S1 and S2 with the maximum at the level of 17 cps/kBq. The effect is a consequence of the smaller radius and larger axial FOV covered by the scanners S4 and S5 with respect to the other setups. The "spikes" visible in the sensitivity profiles correspond to the centers of the strips and the gaps between adjacent rings.

TABLE II

Acceptance (A), factor accounts for the holes and inactive detector components (k), theoretical(S_{theor}) and Monte Carlo-calculated (S_{MC}) sensitivity of the peak of the sensitivity profile.

Type	A[%]	k[%]	S_{theor}[cps/kBq]	S_{MC}[cps/kBq]
S1	60.62	67.29	17.61	19.95
S2	59.23	65.43	17.21	19.50
S3	78.10	84.26	22.69	24.44
S4	79.89	84.41	23.21	26.85
S5	79.89	84.41	30.57	34.24

TABLE III

Number of true, scatter and random coincidences for NEMA IEC and XCAT phantoms.

	NEMA IEC [10^7]			XCAT [10^7]		
Type	True	Scatter	Random	True	Scatter	Random
S1	7.8	4.8	8.1	5.7	3.9	6.0
S2	7.4	4.6	7.7	5.5	3.7	5.8
S3	11.8	7.5	12.2	8.2	6.1	9.1
S4	13.6	8.7	13.9	9.7	7.2	10.6
S5	17.7	11.2	17.6	12.6	9.5	13.5

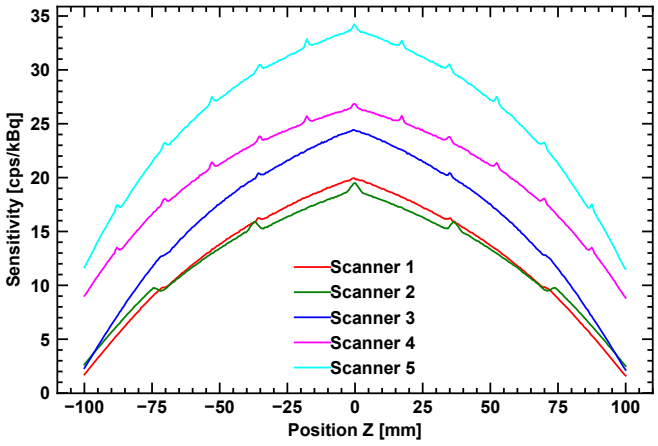

Fig. 8. NEMA sensitivity profiles for tested TB J-PET geometries.

B. Number of coincidences

The numbers of coincidences registered for each scanner and both NEMA IEC and XCAT phantoms are of the order of 10^7 - 10^8 and are given in Table III. The greatest number is found for the S5 scanner and the smallest for the S1 scanner. It is an effect of the increased geometrical acceptance and detector efficiency for thicker (S5 scanner) scintillator layer. The SF and NECR values are given in Table IV. It is found that the S1 and S2 scanners have slightly lower fraction of scattered coincidences compared to the rest of the scanners. The greatest NECR values are found for the S5 and the lowest for the S2 scanners.

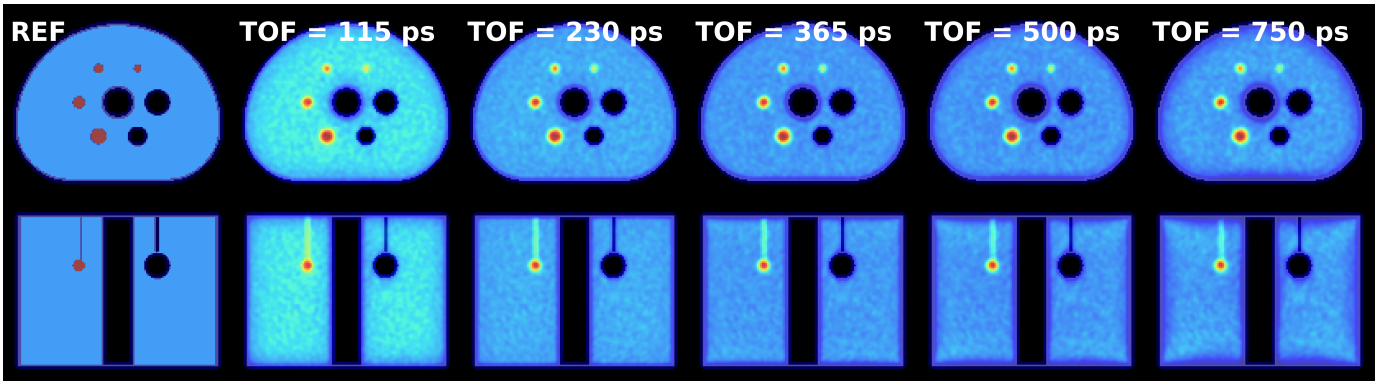

Fig. 9. Simulated (REF label) and reconstructed NEMA IEC images (TOF label) for five different TOF resolutions for the axial (top panel) and sagittal (bottom panel) view. Given slices are for S5. The 30th iteration images are shown. The TOF values indicated in the figures correspond to the values assumed in the reconstruction. In the simulation the value of about σ=77 ps was used.

TABLE IV
SCATTER FRACTION - SF AND NOISE EQUIVALENT COUNT RATE - NECR FOR NEMA IEC AND XCAT PHANTOMS

	SF [%]		NECR [kcps]	
Type	NEMA IEC	XCAT	NEMA IEC	XCAT
S1	38.1	40.4	59.3	34.7
S2	38.2	40.2	55.8	33.8
S3	38.8	42.5	88.7	47.9
S4	38.8	42.8	102.7	56.9
S5	38.8	42.9	134.2	74.6

C. Choice of the optimal TOF kernel

The comparison of the reconstructed images for various Gaussian kernel widths is presented in Fig. 9 and Fig. 10 for the NEMA IEC and XCAT phantoms, respectively. The visual inspection reveals that images obtained with the reconstruction of lower TOF (TOF = 115 ps and TOF = 230 ps) have worse quality than others. Both, the background and noise levels are lower for the images with greater TOF. Furthermore, the contrast between hot regions and the background is more clear for the images with the greater TOF resolution for both, NEMA IEC and XCAT phantoms.

In the Fig. 11 the exemplary Q metric distribution as a function of iteration and applied TOF kernel value is presented for the scanner S5. The Q is calculated for hot spheres (NEMA IEC) and hot spots (XCAT phantom) for 50 iterations and five TOF values. It is found that for all cases the lowest values are observed for the TOF greater than 230 ps. For five out of six cases (excluding hot spot positioned in lungs - XCAT phantom) the lowest (the best) Q are found for the TOF = 365 ps and TOF = 500 ps. The TOF = 115 ps obtained the highest (worse) Q characteristic among all the presented cases. It is also noticeable that for all the images for 50th iteration the Q metric reaches the plateau. The same trend was observed for other scanners.

Taking into account both, the visual inspection and quantitative results, the TOF values between 365 ps to 500 ps could be considered as the optimal kernel width. The shapes of the metric plots are very similar and preserved for all the scanners. In the further image quality analysis, we choose to proceed with the images reconstructed with TOF resolution equal to 500 ps. Detailed analysis of the TOF kernel width selection, together with the full set of plots can be found in the appendix I.

D. Image Quality

1) NEMA IEC phantom: Fig. 12 shows exemplary reconstructed images of the NEMA IEC phantom for all the scanners with TOF resolution equal 500 ps (30th iteration). Hot and cold regions are clearly visible for all the scanners and could be easily distinguished from the background activity. The visual inspection of the images obtained with the S1 and S2 indicates that they are characterized by a greater background noise.

Further analysis were conducted to quantify the CRC, BV, Q and RMSE metrics for simulated NEMA IEC phantom as depicted in Fig. 13 and Fig. 14. Only hot spheres are included in the analysis.

The best CRC values for each hot sphere were observed for various scanners. The CRC values start to reach the plateau from about 40th, 30th, 25th and 20th iterations for spheres with diameter equal 10 mm, 13 mm, 17 mm and 22 mm, respectively. The greater the sphere diameter, the higher CRC values are observed. Note that the differences between the CRC values are relatively small (quantified in Fig. 13), while the CRC uncertainty is mostly similar. Furthermore, the images obtained from all the scanners have similar background variability. Quantitative results differ from visual inspection in terms of the BV metric. The lowest BV is observed for the S4 and S5 scanners. Statistically significant differences are found between the 7 rings and 3 rings scanners.

Q value shows the best results for the biggest sphere. The Q metric is dominated by the CRC. The RMSE characteristic show very small differences (below 2%) between the scanners. Overall, the CRC, Q and RMSE metrices do not give a clear evidence on the superiority of any scanner configuration. However, the BV metric shows advantage of the S4 and S5 scanners over the rest.

2) XCAT phantom: Fig. 15 depicts exemplary reconstructed images of the XCAT phantom for all the scanners with TOF resolution equal to 500 ps (30th iteration). As for the

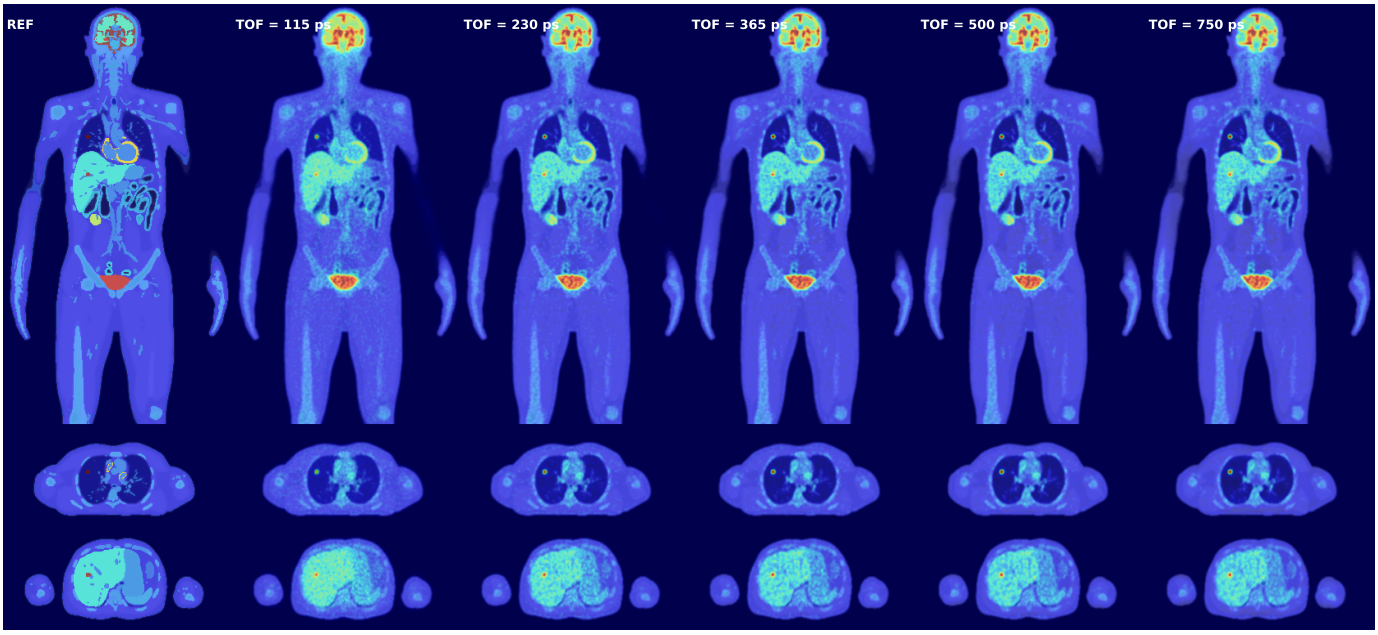

Fig. 10. Simulated (REF label) and reconstructed XCAT phantom images (TOF label) for five different TOF resolutions for the sagittal (top panel) and axial (center and bottom panel) views. Center and bottom panel shows the slice through the hot spot in the lungs and liver, respectively. PET images are overlayed onto CT scans. Given slices are for S5. 30th iteration images are shown. The TOF values indicated in the figures correspond to the values assumed in the reconstruction. In the simulation the value of about σ=77 ps was used.

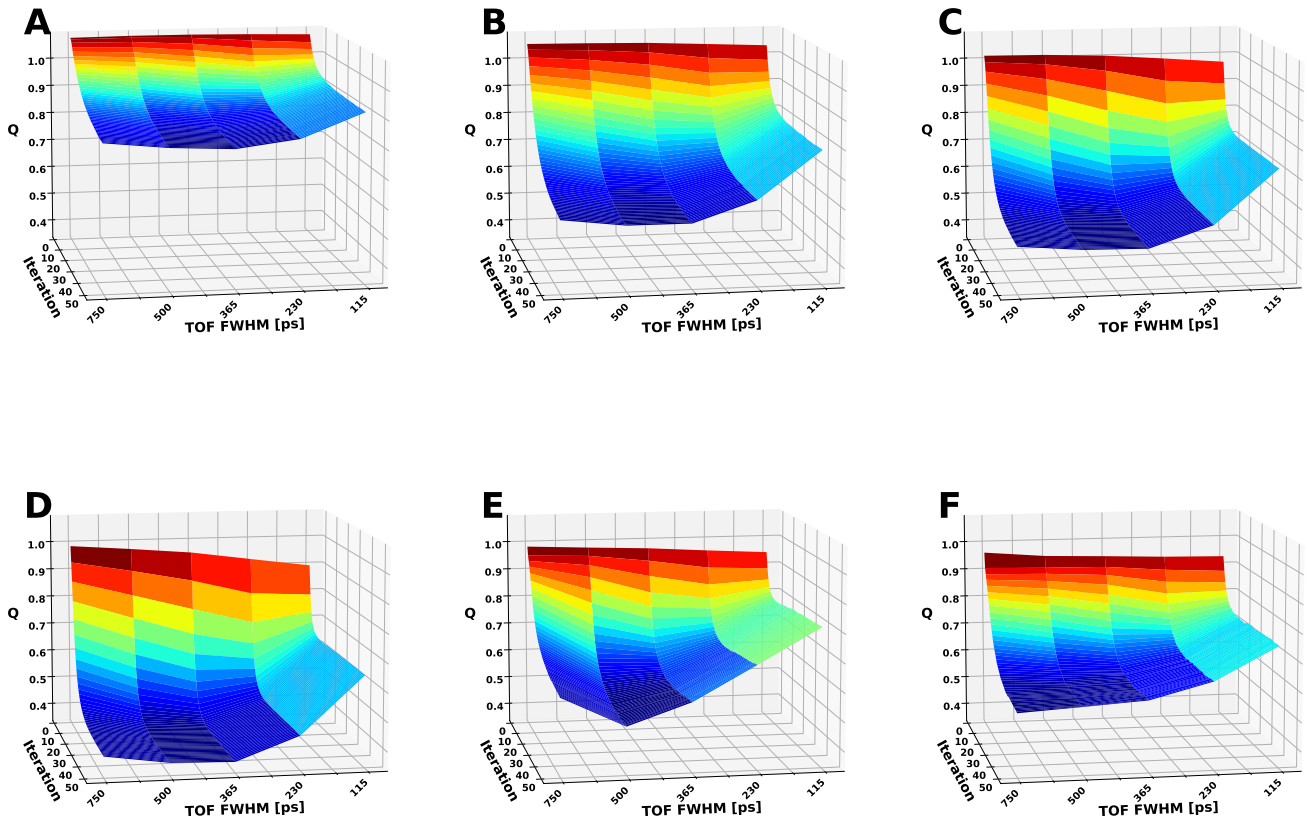

Fig. 11. The Q metric for the NEMA IEC spheres with diameter 10 mm (panel A), 13 mm (panel B), 17 mm (panel C), 22 mm (panel D), and XCAT phantom for lungs (panel E) and liver (panel F) are given. Five tested TOF values are compared for the S5 scanner.

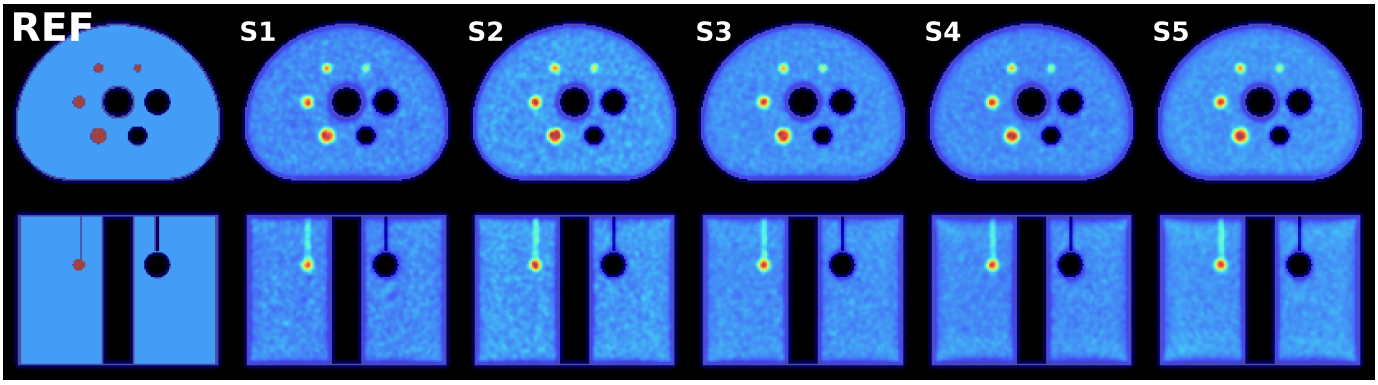

Fig. 12. Simulated (REF label) and reconstructed (S1-S5) NEMA IEC images shown in the axial (top panel) and sagittal (bottom panel) view. For each scanner, the 30th iteration image is shown.

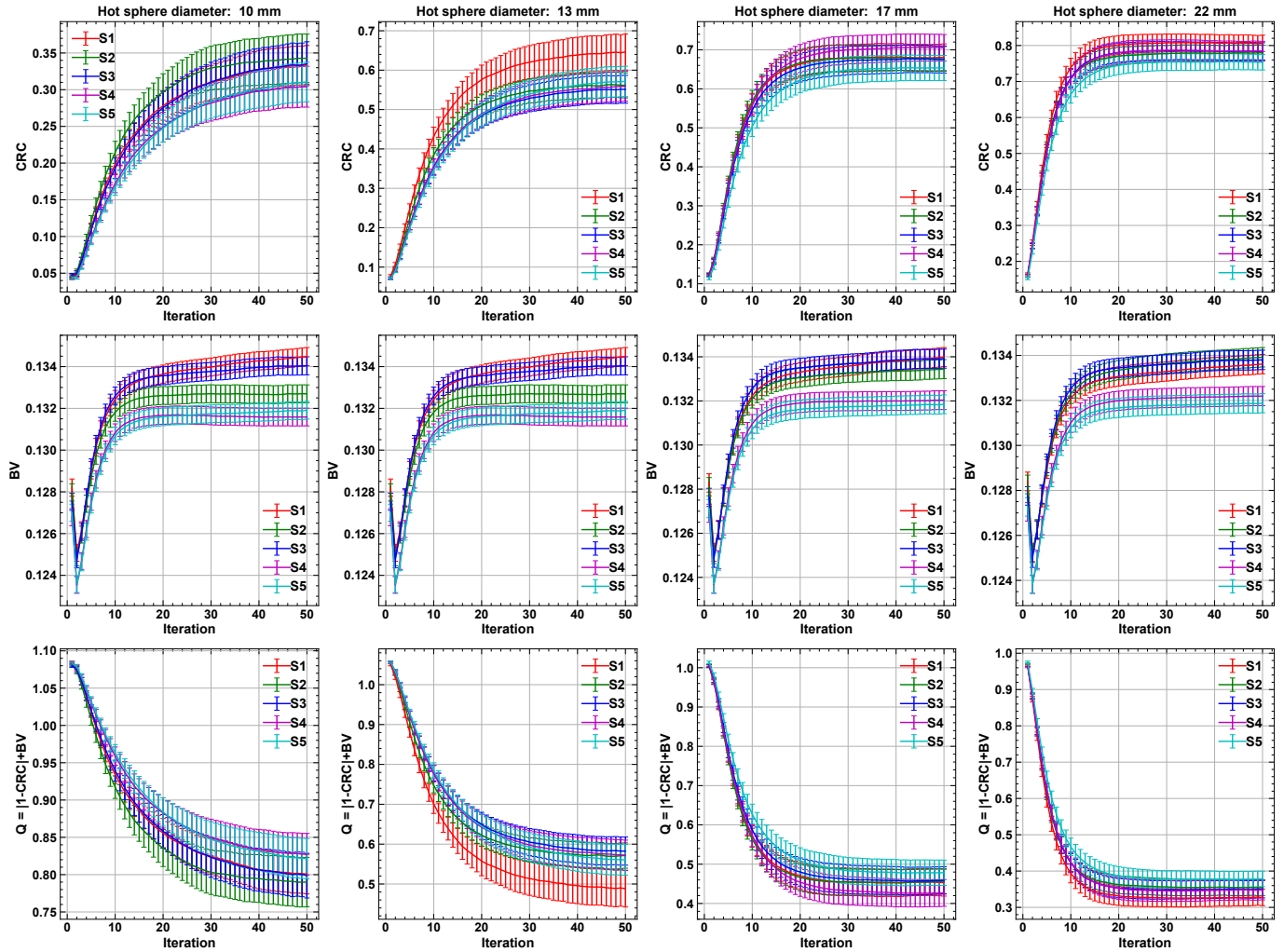

Fig. 13. CRC (top row), BV (middle row) and Q (bottom row) metrics for different scanners with the optimal TOF resolutions equal 500 ps. Four hot spheres with diameters of 10 mm, 13 mm, 17 mm and 22 mm were analyzed.

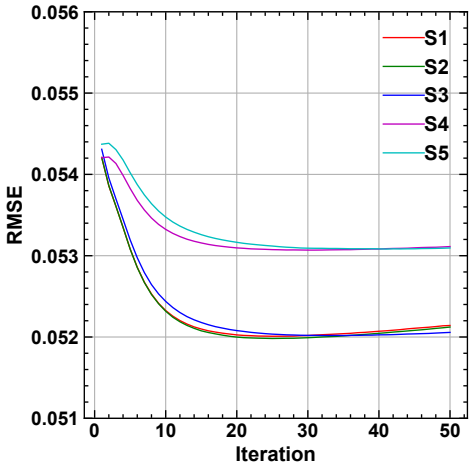

Fig. 14. RMSE characteristics for different scanners. Only the region of the NEMA IEC phantom was analyzed.

NEMA IEC phantom, the visual inspection indicates that the background noise is greater for the S1, S2 and S3 scanners. It is particularly visible in the shoulder girdles and in the axial slices with hot spots in the lungs and the liver. Nevertheless, there is no visual evidence for improved contrast in any of the scanners no in the lungs nor in the liver.

A comprehensive analysis of CRC, BV, Q and RMSE metrics for the reconstructed XCAT images for five scanners is presented in Fig. 16.

The greatest CRC is observed for the lungs, although the CRC variation for each ROI among the scanners does not exceed one standard deviation. Vast discrepancies are observed for the BV metrics. Here, scanners S4 and S5 shows statistically significant superiority for both the liver and the lungs regions over the rest of the scanners. At the same time, the worst results are found for the scanners with the greatest radius - S1 and S2. Above mentioned findings are reflected in the Q metric. As in the case of the BV, the S5 scanner is characterized by the lowest Q metric for both - the liver and the lungs. The same trend is observed for the RMSE metric where the scanner S5 shows an advantage over the results of the other scanners. This can be clearly observed in the liver region. The performance of scanners S1 and S2 is significantly worse than the other scanners. The obtained quantitative results are in agreement with the qualitative, visual inspection.

IV. Discussion

In the presented study sensitivity profiles for five total-body J-PET scanners geometries (Table I) were determined. The peak sensitivity values vary from 20 to 34 cps per kBq, and are dominated by the differences in the geometrical acceptance of the scanners. The maximum peak sensitivity of 34 cps per kBq was found for the scanner S5. This value is slightly lower than the result reported in our previous study [29], where for the 200 cm ideal scanner the sensitivity in peak is equal to 38 cps per kBq. The difference can be explained by the larger radius of the here investigated setup (41.4 cm versus 39 cm) and the inclusion of the gaps between rings and adjacent plastic scintillators. Contrasted with the values reported for the state-of-the-art TB scanners: uExplorer (191.5 cps per kBq) and PennPET (55 cps per kBq) [10], the J-PET scanner sensitivity is lower, however, it can be seen as a significant improvement with respect to the current 16–26 cm long PET systems [61]. The sensitivity of the J-PET scanner can be further increased by adding the third, outer layer of scintillators, which considering the low cost of the plastic scintillators, makes it an attractive solution.

Small differences between SF are observed for all the scanners and NEMA IEC phantom. However, once the activity is more spread in the whole axial FOV (XCAT phantom) the differences between the scanners S1, S2 and scanners S3, S4, S5 become more noticeable. The significant discrepancies in NECR between the scanners were observed. It is caused by the acceptance difference among the scanners. The obtained values are given as indicative for phantoms used. The comparison with external scanners, would require the simulation of the NECR phantom as discussed in norms [51].

The quantitative analysis of the reconstructed image quality was based on simulations of NEMA IEC and XCAT phantoms. The analysis of the reconstructed NEMA IEC phantom images potentially indicate which J-PET TB scanner geometry can be treated as optimal. The CRC values are statistically the same for all the scanners within the estimated uncertainties (see Fig. 13) and the RMSE-based results (see Fig. 14) do not offer the discriminative choice. However, the visual inspection and the differences in BV clearly showed the advantage of S4 and S5 geometries over the other scanners (Fig. 12).

This conclusion is supported by the results from the XCAT study, which show statistically significant differences in the image quality among the investigated J-PET geometries (Fig. 16). As for the NEMA IEC phantom, visual inspection reveals the superiority of the seven-ring scanners (S4 and S5) over the three-ring setups (S1, S2 and S3) (Fig. 15). In particular, the noise level is smaller for the scanners S4 and S5. This is confirmed by the quantitative results shown in Fig. 16. BV value for the S5 is found to be the lowest for both lesions. The CRC values do not give any advantage to a given scanner. In contrast to the NEMA IEC case, BV values are of a similar order as the CRC ones. Thus, both BV and CRC will have similar importance in the Q metric results. For this case, the Q value indicates the scanners S4 and S5 are the optimal geometries for a Total-Body J-PET. Additionally, the RMSE characteristics (for the liver lesions specifically) show the scanner S5 to best mimic the simulated reference image.

In our study, the simulated scenarios uses the same overall activity between investigated scanners and the acquisition time for all the scanners to better reproduce the real conditions. As consequence, the reconstructed images and calculated metrics differ in the number of registered coincidences. It is plausible that the effect of the reduced background variability in the NEMA IEC and XCAT simulation scenarios is observed for the scanners with the highest statistics (S4 and S5).

If we focus on the 2γ + γ_{prompt} coincidences necessary for the positronium imaging technique [16], [61], [62], the estimated S5 scanner sensitivity gain factor is equal to 5 with respect to the current 2γ PET modalities with a typical axial FOV of 20 cm. This makes the J-PET TB modality a well-

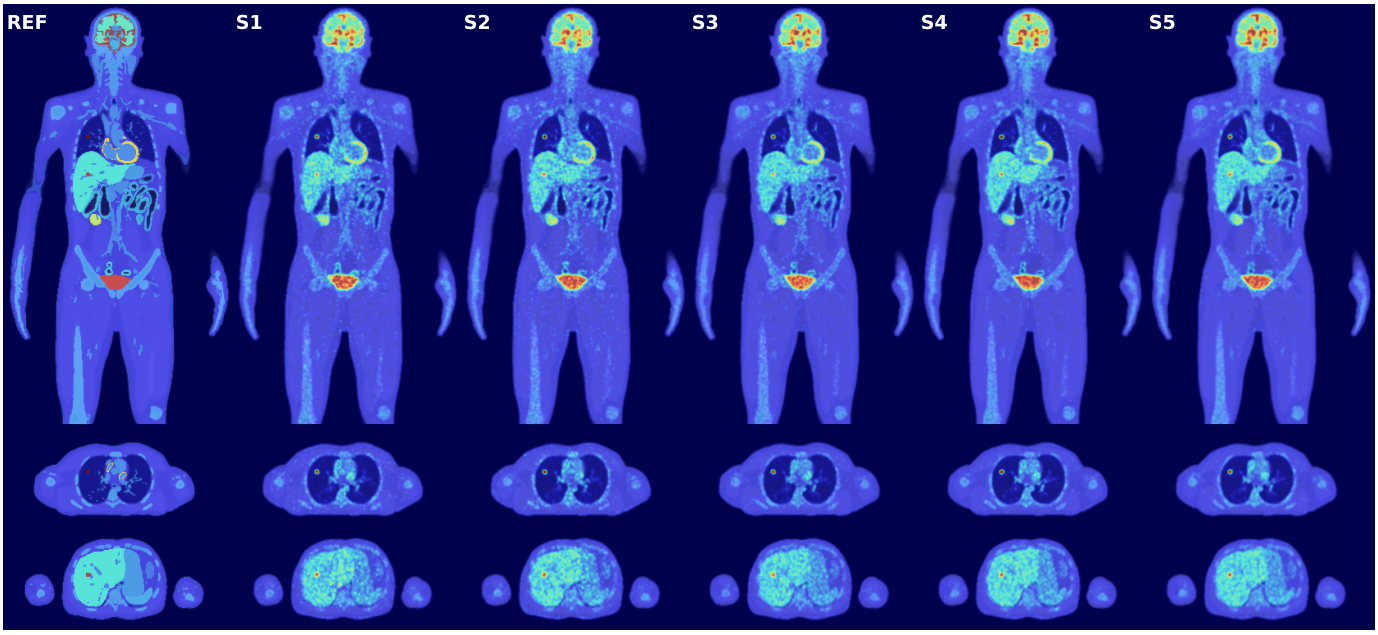

Fig. 15. Simulated (REF panel) and reconstructed (S1-S5) XCAT phantom images for five different scanner types for the sagittal (top panel) and axial (center and bottom panel) views. Center and bottom panel show the slice through the hot spot in lungs and liver, respectively. PET images are overlayed onto CT scans. For each scanner the 30th iteration image is shown.

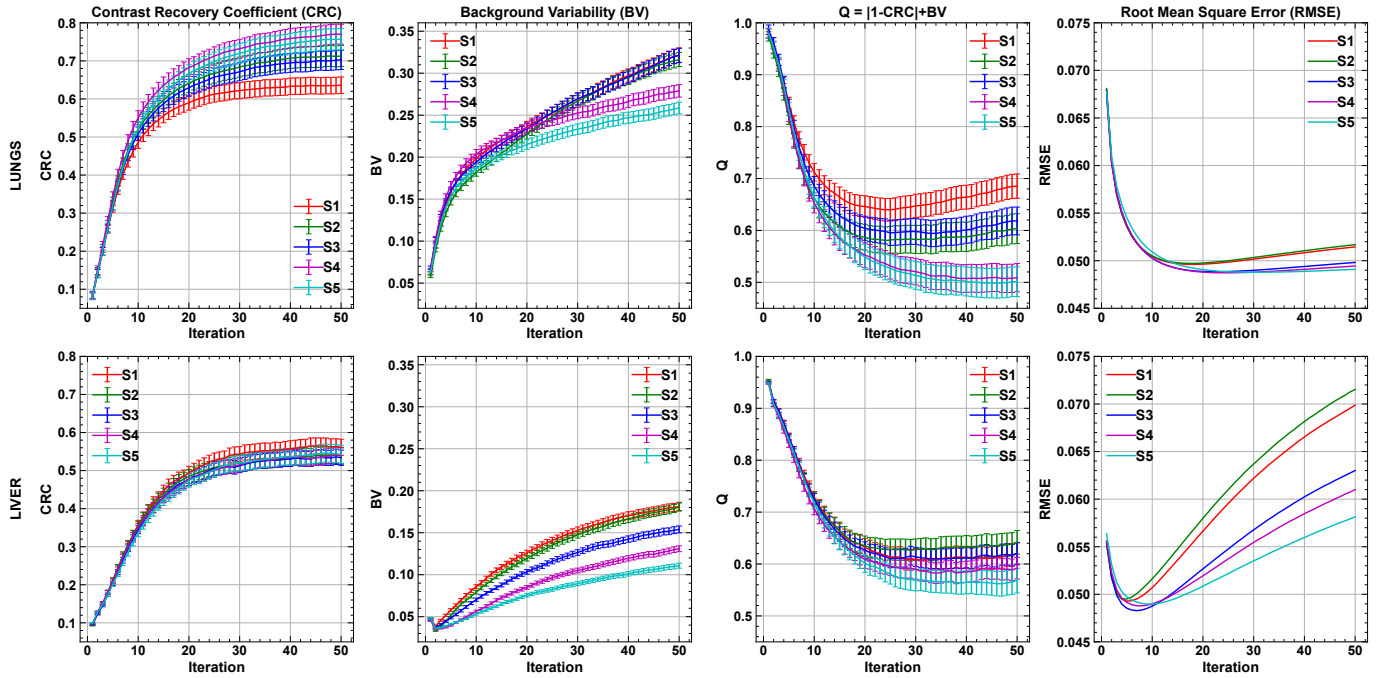

Fig. 16. CRC (first column), BV (second column), Q (third column) and RMSE (fourth column) characteristics for the liver (top row) and lungs (bottom row) regions calculated based on the reconstructed XCAT phantom images for all five scanners.

suited scanner for multi-photon imaging [17], [63].

Note that the presented reconstruction and analysis protocols require further optimization for potential clinical application and it is out of the scope of this paper.

A. Limitations

In the image reconstruction process, the sensitivity and attenuation corrections were included. Image quality could be further improved by the addition of other correction factors such as point spread function (PSF) or depth-of-interaction (DOI) modelling. Indeed, the efforts to develop a dedicated J-PET system response matrix are ongoing [60]. Also, no selection criteria of the obliqueness of the accepted line-of-responses were applied. As it is shown in our previous study, it could improve the contrast and background of the reconstructed images. [64]. However, the more accurate system matrix modelling or application of the obliqueness selection criteria would improve the overall metric values e.g. contrast, but would not change the relative trends we observed among the scanner setups.

In our study, only true coincidences were taken for the image reconstruction. Further studies must be carried out to develop the scatter and random correction methods for the J-PET-based TB scanners.

V. Conclusions

We performed comparative studies of five realistic, two-layer TB J-PET scanners, based on the Monte Carlo simulations of the NEMA IEC and XCAT phantoms.

The overall performance was quantified in terms of sensitivity, SF, NECR, CRC, BV, Q and RMSE metrics. The results show the feasibility of all the systems to be considered for the next generation TB J-PET designs. The analysis of both, NEMA IEC and XCAT simulation results in terms of the quality metrics together with the visual inspection of the reconstructed images point towards the scanner setup S5 (7 rings scanner depicted in Fig. 4) as the optimal design for the final project.

It can be concluded that the image quality increases for the higher sensitivity scanners and it is manifested mainly in the lower background variability values due to the higher statistics. A similar effect was observed in the analysis of the data from the uExplorer TB PET scanner [58].

The obtained sensitivity makes the J-PET TB modality a well-suited scanner for positronium imaging [17]. The enumerated properties together with its cost-effectiveness makes the J-PET technology an attractive solution for the broad application in clinics.

References

[1] McKenney-Drake M. L., Moghbel M.C., Paydary K. et al., "18 f-naf and 18 f-fdg as molecular probes in the evaluation of atherosclerosis," *European journal of nuclear medicine and molecular imaging*, vol. 45, no. 12, pp. 2190–2200, 2018.

[2] Schmall J. P., Karp J. S. and Alavi A., "The potential role of total body pet imaging in assessment of atherosclerosis," *PET clinics*, vol. 14, no. 2, pp. 245–250, 2019.

[3] A. Alavi, T. J. Werner, E. Stępień, and P. Moskal, "Unparalleled and revolutionary impact of pet imaging on research and day to day practice of medicine," *Bio-Algorithms and Med-Systems*, vol. 17, no. 4, pp. 203–212, 2021.

[4] A. Alavi, S. Hess, T. J. Werner, and P. F. Høilund-Carlsen, "An update on the unparalleled impact of fdg-pet imaging on the day-to-day practice of medicine with emphasis on management of infectious/inflammatory disorders," pp. 18–27, 2020.

[5] Cherry S. R., Badawi R. D., Karp J. S. et al., "Total-body imaging: Transforming the role of positron emission tomography," *Science Translational Medicine*, vol. 9, no. 381, 2017.

[6] B. A. Spencer, E. Berg, J. P. Schmall, N. Omidvari, E. K. Leung, Y. G. Abdelhafez, S. Tang, Z. Deng, Y. Dong, Y. Lv *et al.*, "Performance evaluation of the uexplorer total-body pet/ct scanner based on nema nu 2-2018 with additional tests to characterize pet scanners with a long axial field of view," *Journal of Nuclear Medicine*, vol. 62, no. 6, pp. 861–870, 2021.

[7] Karp J. S., Viswanath V., Geagan M. J. et al., "Pennpet explorer: design and preliminary performance of a whole-body imager," *Journal of Nuclear Medicine*, vol. 61, no. 1, pp. 136–143, 2020.

[8] I. Alberts, J.-N. Hünermund, G. Prenosil, C. Mingels, K. P. Bohn, M. Viscione, H. Sari, B. Vollnberg, K. Shi, A. Afshar-Oromieh *et al.*, "Clinical performance of long axial field of view pet/ct: a head-to-head intra-individual comparison of the biograph vision quadra with the biograph vision pet/ct," *European journal of nuclear medicine and molecular imaging*, vol. 48, no. 8, pp. 2395–2404, 2021.

[9] G. A. Prenosil, H. Sari, M. Fürstner, A. Afshar-Oromieh, K. Shi, A. Rominger, and M. Hentschel, "Performance characteristics of the biograph vision quadra pet/ct system with a long axial field of view using the nema nu 2-2018 standard," *Journal of nuclear medicine*, vol. 63, no. 3, pp. 476–484, 2022.

[10] S. Vandenberghe, P. Moskal, and J. S. Karp, "State of the art in total body pet," *EJNMMI physics*, vol. 7, no. 1, pp. 1–33, 2020.

[11] S. Vandenberghe, N. A. Karakatsanis, M. A. Akl, J. Maebe, S. Surti, R. A. Dierckx, D. A. Pryma, S. A. Nehmeh, O. Bouhali, and J. S. Karp, "The potential of a medium-cost long axial fov pet system for nuclear medicine departments," *European Journal of Nuclear Medicine and Molecular Imaging*, pp. 1–9, 2022.

[12] X. Zhang, Z. Xie, E. Berg, M. S. Judenhofer, W. Liu, T. Xu, Y. Ding, Y. Lv, Y. Dong, Z. Deng *et al.*, "Total-body dynamic reconstruction and parametric imaging on the uexplorer," *Journal of Nuclear Medicine*, vol. 61, no. 2, pp. 285–291, 2020.

[13] G. Wang, L. Nardo, M. Parikh, Y. G. Abdelhafez, E. Li, B. A. Spencer, J. Qi, T. Jones, S. R. Cherry, and R. D. Badawi, "Total-body pet multiparametric imaging of cancer using a voxelwise strategy of compartmental modeling," *Journal of Nuclear Medicine*, vol. 63, no. 8, pp. 1274–1281, 2022.

[14] Y. Wang, E. Li, S. R. Cherry, and G. Wang, "Total-body pet kinetic modeling and potential opportunities using deep learning," *PET clinics*, vol. 16, no. 4, pp. 613–625, 2021.

[15] E. J. Li, B. A. Spencer, J. P. Schmall, Y. Abdelhafez, R. D. Badawi, G. Wang, and S. R. Cherry, "Efficient delay correction for total-body pet kinetic modeling using pulse timing methods," *Journal of Nuclear Medicine*, vol. 63, no. 8, pp. 1266–1273, 2022.

[16] P. Moskal, K. Dulski, N. Chug, C. Curceanu, E. Czerwiński, M. Dadgar, J. Gajewski, A. Gajos, G. Grudzień, B. C. Hiesmayr *et al.*, "Positronium imaging with the novel multiphoton pet scanner," *Science Advances*, vol. 7, no. 42, p. eabh4394, 2021.

[17] P. Moskal and E. Ł. Stępień, "Perspectives for translation of positronium imaging into clinics," *Frontiers in Physics*, p. 891, 2022.

[18] Moskal P., Kisielewska D., Curceanu C. et al., "Feasibility study of the positronium imaging with the J-PET tomograph," *Physics in Medicine and Biology*, vol. 64, no. 5, p. 055017, 2019.

[19] Cherry S. R., Jones T., Karp J. S. et al., "Total-Body PET: Maximizing Sensitivity to Create New Opportunities for Clinical Research and Patient Care," *The Journal of Nuclear Medicine*, vol. 59, no. 1, pp. 3–12, 2018.

[20] Surti S., Pantel A. R. and Karp J. S., "Total body pet: Why, how, what for?" *IEEE Transactions on Radiation and Plasma Medical Sciences*, vol. 4, no. 3, pp. 283–292, 2020.

[21] Surti S., Werner M. E. and Karp J. S., "Study of pet scanner designs using clinical metrics to optimize the scanner axial fov and crystal thickness," *Physics in Medicine and Biology*, vol. 58, no. 12, p. 3995, 2013.

[22] Zhang J., Knopp M. I. and Knopp M. V., "Sparse detector configuration in sipm digital photon counting pet: a feasibility study," *Molecular Imaging and Biology*, vol. 21, no. 3, pp. 447–453, 2019.

[23] Zein S. A., Karakatsanis N. A., Issa M. et al., "Physical performance of a long axial field-of-view pet scanner prototype with sparse rings configuration: A monte carlo simulation study," *Medical Physics*, vol. 47, no. 4, pp. 1949–1957, 2020.

[24] Brunner S. E. and Schaart D. R., "Bgo as a hybrid scintillator/cherenkov radiator for cost-effective time-of-flight pet," *Physics in Medicine and Biology*, vol. 62, no. 11, p. 4421, 2017.

[25] Kwon S. I., Roncali E., Gola A. et al., "Dual-ended readout of bismuth germanate to improve timing resolution in time-of-flight pet," *Physics in Medicine and Biology*, vol. 64, no. 10, p. 105007, 2019.

[26] Cates J. W. and Levin C. S., "Electronics method to advance the coincidence time resolution with bismuth germanate," *Physics in Medicine and Biology*, vol. 64, no. 17, p. 175016, 2019.

[27] Gundacker S., Turtos R. M., Kratochwil N., et al., "Experimental time resolution limits of modern sipms and tof-pet detectors exploring different scintillators and cherenkov emission," *Physics in Medicine and Biology*, vol. 65, no. 2, p. 025001, 2020.

[28] Kowalski P., Wiślicki W., Shopa R. Y. et al., "Estimating the NEMA characteristics of the J-PET tomograph using the GATE package," *Physics in Medicine and Biology*, vol. 63, p. 165008, 2018.

[29] P. Moskal, P. Kowalski, R. Shopa, L. Raczyński, J. Baran, N. Chug, C. Curceanu, E. Czerwiński, M. Dadgar, K. Dulski *et al.*, "Simulating nema characteristics of the modular total-body j-pet scanner—an economic total-body pet from plastic scintillators," *Physics in Medicine & Biology*, vol. 66, no. 17, p. 175015, 2021.

[30] Lang C., Habs D., Parodi K. and Thirolf P. G., "Sub-millimeter nuclear medical imaging with high sensitivity in positron emission tomography using β+ γ coincidences," *Journal of Instrumentation*, vol. 9, no. 01, p. P01008, 2014.

[31] Thirolf P. G., Lang C. and Parodi K., "Perspectives for highly-sensitive pet-based medical imaging using β+ γ coincidences." *Acta Physica Polonica, A.*, vol. 127, no. 5, 2015.

[32] Yoshida E., Tashima H., Nagatsu K. et al., "Whole gamma imaging: a new concept of PET combined with Compton imaging," *Physics in Medicine and Biology*, vol. 65, no. 12, p. 125013, 2020.

[33] K. Shimazoe, M. Yoshino, Y. Ohshima, M. Uenomachi, K. Oogane, T. Orita, H. Takahashi, K. Kamada, A. Yoshikawa, and M. Takahashi, "Development of simultaneous pet and compton imaging using gagg-sipm based pixel detectors," *Nuclear Instruments and Methods in Physics Research Section A: Accelerators, Spectrometers, Detectors and Associated Equipment*, vol. 954, p. 161499, 2020.

[34] H. Hemmati, A. Kamali-Asl, M. Ay, and P. Ghafarian, "Compton scatter tomography in tof-pet," *Physics in Medicine & Biology*, vol. 62, no. 19, p. 7641, 2017.

[35] A. Kishimoto, J. Kataoka, T. Taya, L. Tagawa, S. Mochizuki, S. Ohsuka, Y. Nagao, K. Kurita, M. Yamaguchi, N. Kawachi *et al.*, "First demonstration of multi-color 3-d in vivo imaging using ultra-compact compton camera," *Scientific reports*, vol. 7, no. 1, pp. 1–7, 2017.

[36] M. Uenomachi, Y. Mizumachi, Y. Yoshihara, H. Takahashi, K. Shimazoe, G. Yabu, H. Yoneda, S. Watanabe, S. Takeda, T. Orita *et al.*, "Double photon emission coincidence imaging with gagg-sipm compton camera," *Nuclear Instruments and Methods in Physics Research Section A: Accelerators, Spectrometers, Detectors and Associated Equipment*, vol. 954, p. 161682, 2020.

[37] H. Tashima and T. Yamaya, "Compton imaging for medical applications," *Radiological Physics and Technology*, pp. 1–19, 2022.

[38] K. Parodi, T. Yamaya, and P. Moskal, "Experience and new prospects of pet imaging for ion beam therapy monitoring," *Zeitschrift für Medizinische Physik*, 2022.

[39] L. Raczyński, W. Wiślicki, W. Krzemień, P. Kowalski, D. Alfs, T. Bednarski, P. Białas, C. Curceanu, E. Czerwiński, K. Dulski *et al.*, "Calculation of the time resolution of the j-pet tomograph using kernel density estimation," *Physics in Medicine & Biology*, vol. 62, no. 12, p. 5076, 2017.

[40] P. Moskal *et al.*, "Testing CPT symmetry in ortho-positronium decays with positronium annihilation tomography," *Nature Commun.*, vol. 12, no. 1, p. 5658, 2021.

[41] Hiesmayr B. C. and Moskal P., "Witnessing entanglement in Compton scattering processes via mutually unbiased bases," *Scientific reports*, vol. 9, no. 1, pp. 1–14, 2019.

[42] J. Baran, J. Gajewski, M. Pawlik-Niedźwiecka, P. Moskal, and A. Ruciński, "Studies of j-pet detector to monitor range uncertainty in proton therapy," in *2019 IEEE Nuclear Science Symposium and Medical Imaging Conference (NSS/MIC)*. IEEE, 2019, pp. 1–4.

[43] D. Borys, J. Baran, K. Brzeinski, J. Gajewsk, N. Chug, A. Coussat, E. Czerwiński, M. Dadgar, K. Dulski, K. V.Eliyan, A. Gajos, K. Kacprzak, Ł. Kapłon, K. Klimaszewski, P. Konieczka, R. Kopeć, G. Korcyl, T. Kozik, W. Krzemień, D. Kumar, A. J.Lomax, K. McNamara, S. Niedźwiecki, P. Olko, D. Panek, S. Parzych, E. Perez del Rio, L. Raczyński, S. Sharma, Shivani, R. Y. Shopa, T. Skóra, M. Skurzok, P. Stasica, E. Ł. Stępień, K. Tayefi, F. Tayefi, D. C.Weber, C. Winterhalter, W. Wiślicki, P.s Moskal, and A. Rucinski, "ProTheRaMon - A GATE simulation framework for proton therapy range monitoring using PET imaging," *Accepted by Physics in Medicine and Biology*, 2022.

[44] R. Y. Shopa, K. Klimaszewski, P. Kopka, P. Kowalski, W. Krzemień, L. Raczyński, W. Wiślicki, N. Chug, C. Curceanu, E. Czerwiński *et al.*, "Optimisation of the event-based tof filtered back-projection for online imaging in total-body j-pet," *Medical Image Analysis*, vol. 73, p. 102199, 2021.

[45] L. Raczyński, W. Wiślicki, K. Klimaszewski, W. Krzemień, P. Kopka, P. Kowalski, R. Shopa, M. Bała, J. Chhokar, C. Curceanu *et al.*, "3d tof-pet image reconstruction using total variation regularization," *Physica Medica*, vol. 80, pp. 230–242, 2020.

[46] S. Niedźwiecki, P. Białas, C. Curceanu, E. Czerwiński, K. Dulski, A. Gajos, B. Głowacz, M. Gorgol, B. Hiesmayr, B. Jasińska *et al.*, "J-pet: a new technology for the whole-body pet imaging," *arXiv preprint arXiv:1710.11369*, 2017.

[47] Smyrski J., Alfs D., Bednarski T. et al., "Measurement of gamma quantum interaction point in plastic scintillator with WLS strips," *Nucl. Instrum. Meth.*, vol. A851, pp. 39–42, 2017.

[48] D. Sarrut, M. Bała, M. Bardiès, J. Bert, M. Chauvin, K. Chatzipapas, M. Dupont, A. Etxebeste, L. M. Fanchon, S. Jan *et al.*, "Advanced monte carlo simulations of emission tomography imaging systems with gate," *Physics in Medicine & Biology*, vol. 66, no. 10, p. 10TR03, 2021.

[49] D. Sarrut, T. Baudier, D. Borys, A. Etxebeste, H. Fuchs, J. Gajewski, L. Grevillot, S. Jan, G. C. Kagadis, H. G. Kang *et al.*, "The opengate ecosystem for monte carlo simulation in medical physics," *Physics in Medicine & Biology*, 2022.

[50] S. Agostinelli, J. Allison, K. a. Amako, J. Apostolakis, H. Araujo, P. Arce, M. Asai, D. Axen, S. Banerjee, G. Barrand *et al.*, "Geant4—a simulation toolkit," *Nuclear instruments and methods in physics research section A: Accelerators, Spectrometers, Detectors and Associated Equipment*, vol. 506, no. 3, pp. 250–303, 2003.

[51] NEMA, "Nema standards publication nu 2-2018: Performance measurements of positron emission tomographs (pet)," 2018, national Electrical Manufacturers Association (NEMA NU 2-2018).

[52] W. P. Segars, G. Sturgeon, S. Mendonca, J. Grimes, and B. M. Tsui, "4d xcat phantom for multimodality imaging research," *Medical physics*, vol. 37, no. 9, pp. 4902–4915, 2010.

[53] S. Zincirkeser, E. Şahin, M. Halac, and S. Sager, "Standardized uptake values of normal organs on 18f-fluorodeoxyglucose positron emission tomography and computed tomography imaging," *Journal of international medical research*, vol. 35, no. 2, pp. 231–236, 2007.

[54] J. Silva-Rodríguez, P. Aguiar, I. Domínguez-Prado, P. Fierro, and Á. Ruibal, "Simulated fdg-pet studies for the assessment of suv quantification methods," *Revista Española de Medicina Nuclear e Imagen Molecular (English Edition)*, vol. 34, no. 1, pp. 13–18, 2015.

[55] P. Moskal *et al.*, "Test of a single module of the J-PET scanner based on plastic scintillators," *Nucl. Instrum. Meth.*, vol. A764, pp. 317–321, 2014.

[56] Moskal P., Alfs D., Bednarski T. et al., "Potential of the J-PET detector for studies of discrete symmetries in decays of positronium atom-a purely leptonic system," *Acta Phys. Polon.*, vol. B47, p. 509, 2016.

[57] Moskal P., Krawczyk N., Hiesmayr B. C. et al., "Feasibility studies of the polarization of photons beyond the optical wavelength regime with the J-PET detector," *The European Physical Journal C*, vol. 78, no. 11, p. 970, 2018.

[58] X. Zhang, J. Zhou, S. R. Cherry, R. D. Badawi, and J. Qi, "Quantitative image reconstruction for total-body pet imaging using the 2-meter long explorer scanner," *Physics in Medicine & Biology*, vol. 62, no. 6, p. 2465, 2017.

[59] T. Merlin, S. Stute, D. Benoit, J. Bert, T. Carlier, C. Comtat, M. Filipovic, F. Lamare, and D. Visvikis, "Castor: a generic data organization and processing code framework for multi-modal and multi-dimensional tomographic reconstruction," *Physics in Medicine & Biology*, vol. 63, no. 18, p. 185005, 2018.

[60] R. Y. Shopa, J. Baran, K. Klimaszewski, W. Krzemien, L. Raczynski, W. Wislicki *et al.*, "TOF MLEM Adaptation for the Total-Body J-PET with a Realistic Analytical System Response Matrix," *Submitted to IEEE Transactions on Radiation and Plasma Medical Sciences*, 2022.

[61] Moskal P., Kisielewska D., Shopa R. Y. et al., "Performance assessment of the 2 γ positronium imaging with the total-body pet scanners," *EJNMMI Phys.*, vol. 7, p. 44, 2020.

[62] K. Shibuya, H. Saito, F. Nishikido, M. Takahashi, and T. Yamaya, "Oxygen sensing ability of positronium atom for tumor hypoxia imaging," *Communications Physics*, vol. 3, no. 1, pp. 1–8, 2020.
[63] P. Moskal and E. Stępień, "Prospects and clinical perspectives of total-body pet imaging using plastic scintillators," *PET clinics*, vol. 15, no. 4, pp. 439–452, 2020.
[64] P. Kopka and K. Klimaszewski, "Reconstruction of the nema iec body phantom from j-pet total-body scanner simulation using stir." *Acta Physica Polonica B*, vol. 51, no. 1, 2020.

Appendix I
Estimation of the optimal TOF kernel

In this appendix we discuss the selection of the optimal shift-invariant, gaussian TOF kernel width, which was used during the image reconstruction process. The CASToR software provides the possibility to use the shift-invariant TOF kernel only. This approach can be sub-optimal, especially while dealing with the large FOV scanners, where the kernel shape can change significantly in the axial direction [60]. Due to the peculiarity of the J-PET scanner, the optimal width of the shift-invariant Gaussian kernel should be larger than the one determined by the nominal TOF resolution, because of the additional uncertainty of the hit registration position along the axial direction of the strip that effectively smears the overall TOF resolution. Therefore, we performed an investigation to choose the optimal shift-invariant Gaussian kernel width.

A. Distributions as functions of TOF kernel width

Quantitative analysis of the TOF influence on the image quality for the NEMA IEC phantom is shown in Fig. 17 and Fig. 18 where CRC, BV, Q and RMSE metrics are calculated for each scanner and TOF for the 50^{th} iteration. The CRC for the NEMA IEC phantom achieves the plateau starting from the TOF = 365 ps. The trend is visible for all the scanners and four ROIs. The CRC values decrease slightly for the TOF = 750 ps with respect to the TOF = 365 ps and TOF = 500 ps. However, the uncertainties analysis shows that there is no difference in contrast between the images obtained with TOF = 365 ps, TOF = 500 ps and TOF = 750 ps for each scanner. On the other hand, the BV values increase and reach the maximum for the TOF = 365 ps and after that decrease again. Considering the uncertainties, the BV values are equal within one standard deviation for the S4 and S5 for TOF = 230 ps and TOF = 365 ps.

Looking at the Q characteristics it could be found that for three TOF values of 365 ps, 500 ps and 700 ps, the results are similar and Q is lower than for 230 ps and 115 ps. However, it has to be clarified to the Reader that CRC values are much higher and thus they dominate the Q metric (see Eq. 8). The greater the ROI is, the more significant influence of CRC on Q is noticed. It is also seen when uncertainties are considered, there are no significant differences between Q metric for the images reconstructed with the three greatest TOF. The RMSE results are consistent across all the scanners. The best (lowest) values are observed for TOF = 230 ps. It is also found that the scanners with greater axial FOV (S4 and S5) obtained slightly worse results with respect to the other scanners. This might be an effect of the acceptance of more oblique LORs compared to the other scanners.

Complementary results for the XCAT phantom are also presented in Fig. 19. Here, the analysis for two regions was performed: lungs and liver. The CRC characteristics varied between the two regions. For the lungs, it is found that the greatest contrast is achieved for the TOF = 500 ps and TOF = 750 ps. Contrary, for the liver ROI, the CRC plateau is visible starting from the TOF = 365 ps. For lower TOF resolutions, the CRC is decreasing. However, considering the uncertainties, for the lungs images reconstructed with TOF = 500 ps and TOF = 750 ps have statistically the same CRC values. For the liver also TOF = 365 ps do not show any statistical differences with respect to the images obtained with TOF = 500 ps and TOF = 750 ps. The BV characteristic also vary between the regions. In general, the greater TOF resolution, the higher BV is found for the lungs. Statistically different BV metrics are observed for all TOFs. The level of the BV values is similar to the CRC which makes the Q value more affected by both values. It is found that for that case, the Q metric is the best for the TOF = 500 ps for all scanners and statistical difference is proven. On the other hand, for the liver ROI, an almost constant BV level (0.1-0.2 for all scanners) is observed starting from the 365 ps. Here, the Q metric is dominated by the CRC and the best values are observed for the images reconstructed with the TOF = 500 ps and TOF = 750 ps. However, once the uncertainties are considered images with TOF greater than 115 ps revealed the same Q statistics. Significantly different behaviour of the RMSE between lungs and liver is observed. The minimum for TOF = 230 ps is found for the liver ROI whereas the increasing trend (with an increased TOF resolution) is observed for the lungs for all the scanners.

B. Q metric distributions as functions of iteration and TOF kernel width

The Q metric distributions as a function of iteration and applied TOF kernel width value are presented for four scanners (S1-S4). The corresponding plot is shown in Fig. 11.

In the all cases the TOF values between 365 ps to 500 ps could be considered as the optimal kernel width. The shapes of the metric plots are very similar and preserved for all the scanners.

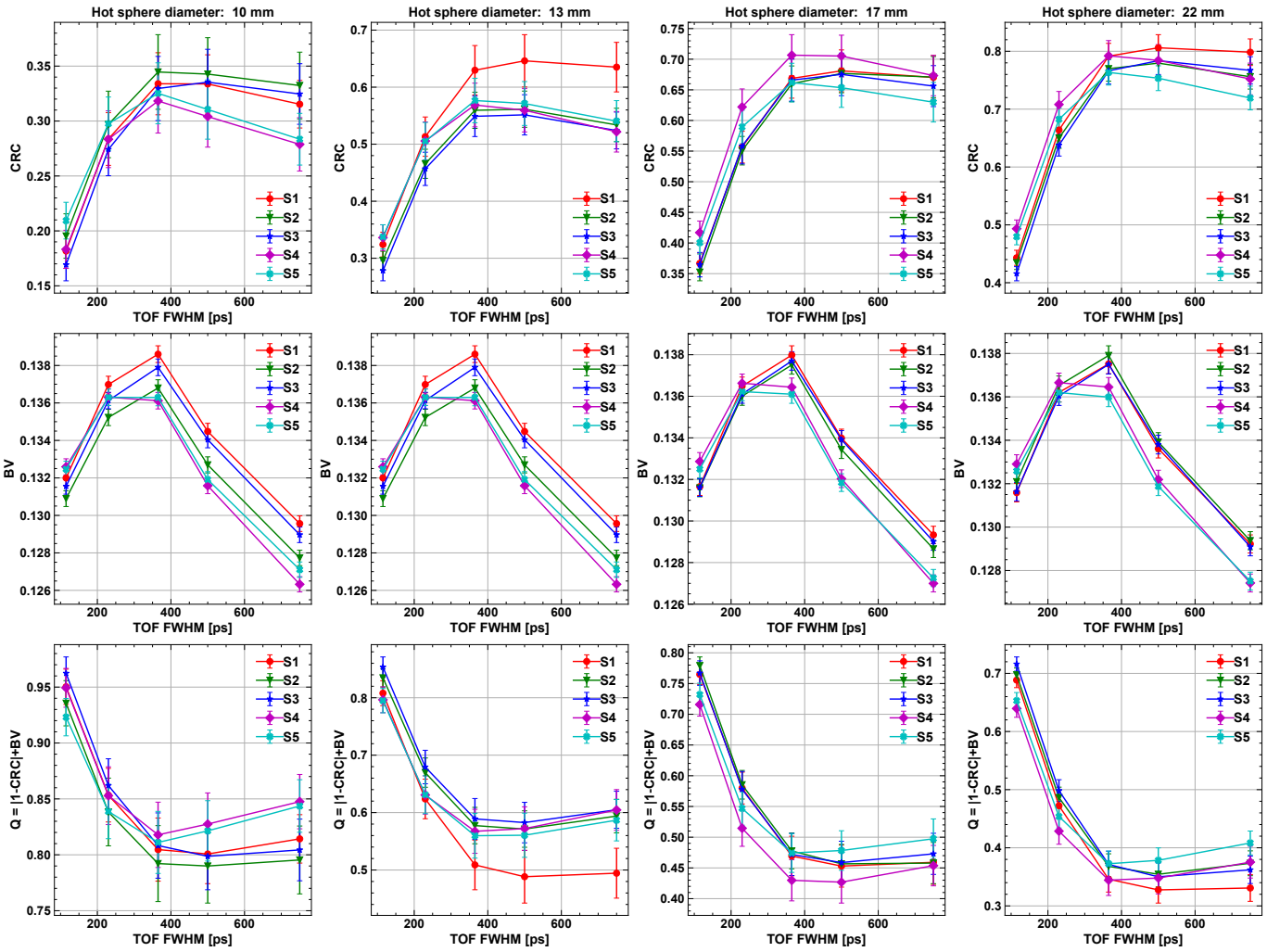

Fig. 17. CRC (top panel), BV (middle panel) and Q (bottom panel) metrics for TOF resolutions 115 ps, 230 ps, 365 ps, 500 ps and 750 ps and hot spheres diameters of 10 mm, 13 mm, 17 mm and 22 mm (from left to right). Metrics were calculated based on the images from the 50th iteration.

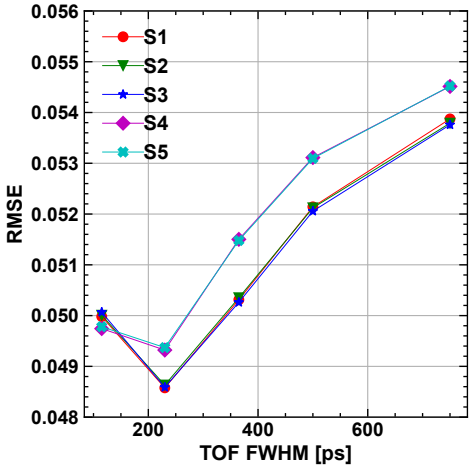

Fig. 18. RMSE metrics as a function of TOF resolution (115 ps, 230 ps, 365 ps, 500 ps and 750 ps). The region of the NEMA IEC phantom was analyzed only. Metrics were calculated based on the images from the 50th iteration.

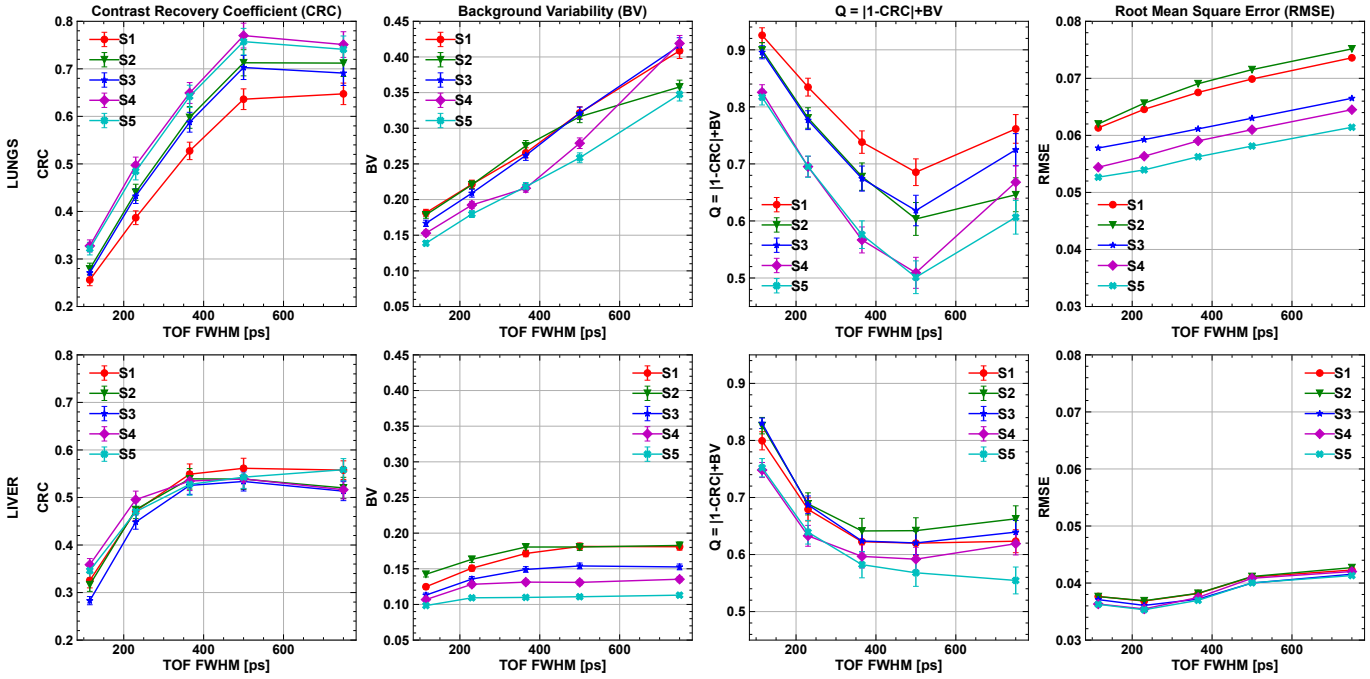

Fig. 19. CRC (first column), BV (second column), Q (third column) and RMSE (fourth column) metrics for different TOF resolutions 115 ps, 230 ps, 365 ps, 500 ps and 750 ps for liver (top panel) and lungs(bottom panel) calculated from the reconstructed XCAT phantom image. Metrics were calculated based on the images from the 50th iteration.

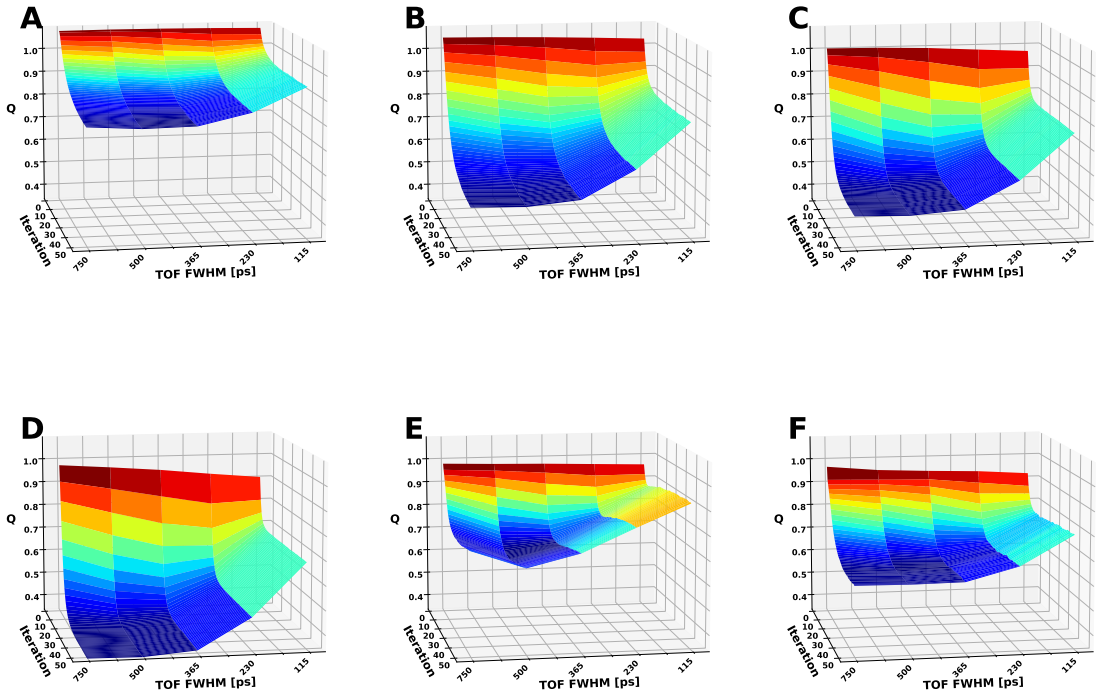

Fig. 20. The Q metric for the NEMA IEC spheres with diameter 10 mm (panel A), 13 mm (panel B), 17 mm (panel C), 22 mm (panel D), and XCAT phantom for lungs (panel E) and liver (panel F) are given. Five tested TOF values are compared for the S1 scanner.

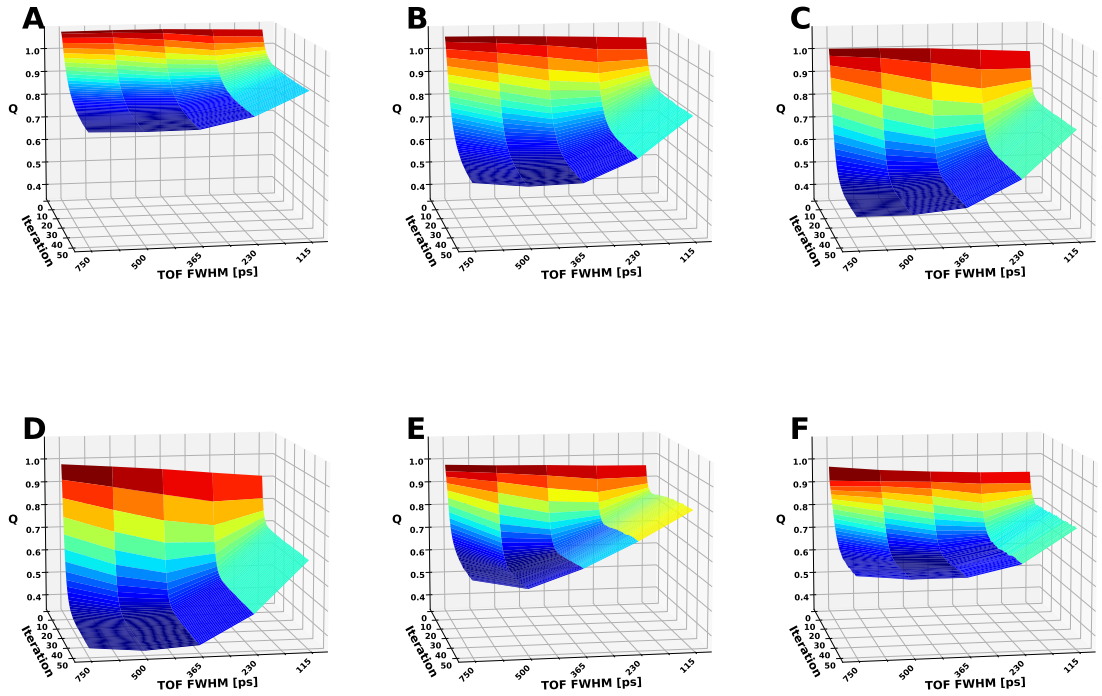

Fig. 21. The Q metric for the NEMA IEC spheres with diameter 10 mm (panel A), 13 mm (panel B), 17 mm (panel C), 22 mm (panel D), and XCAT phantom for lungs (panel E) and liver (panel F) are given. Five tested TOF values are compared for the S2 scanner.

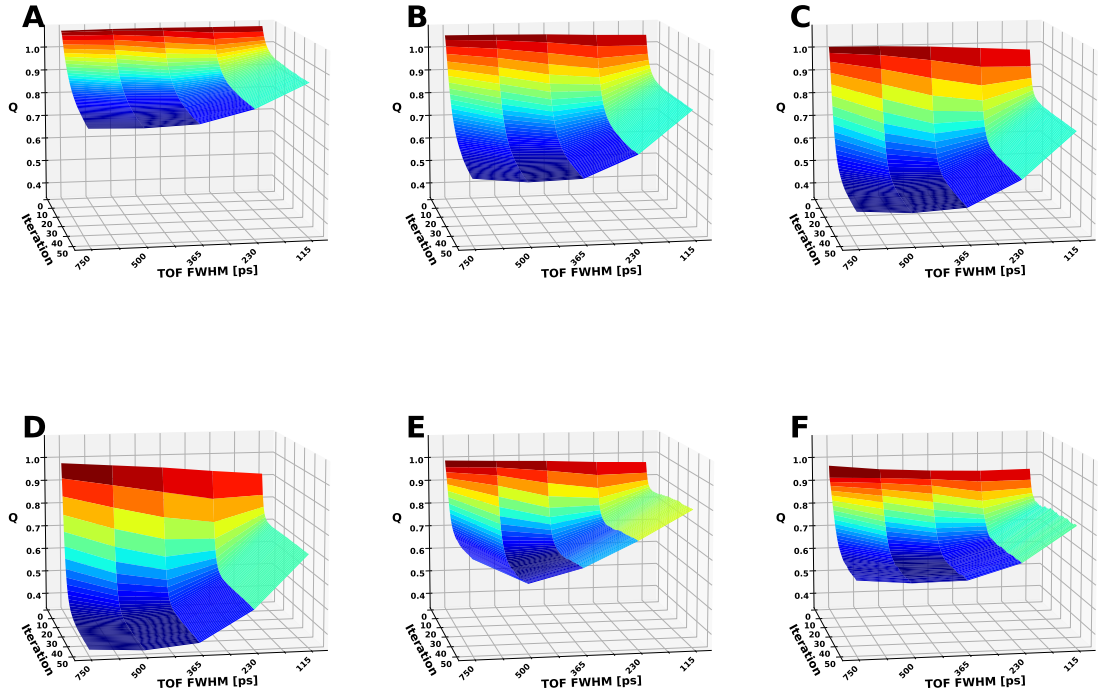

Fig. 22. The Q metric for the NEMA IEC spheres with diameter 10 mm (panel A), 13 mm (panel B), 17 mm (panel C), 22 mm (panel D), and XCAT phantom for lungs (panel E) and liver (panel F) are given. Five tested TOF values are compared for the S3 scanner.

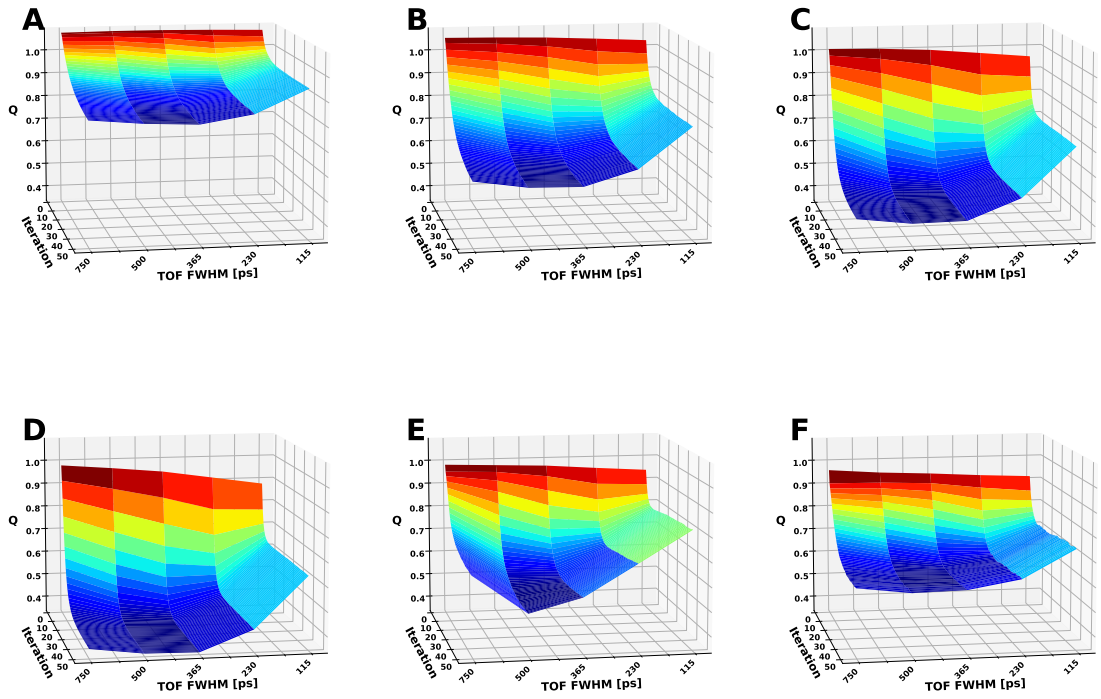

Fig. 23. The Q metric for the NEMA IEC spheres with diameter 10 mm (panel A), 13 mm (panel B), 17 mm (panel C), 22 mm (panel D), and XCAT phantom for lungs (panel E) and liver (panel F) are given. Five tested TOF values are compared for the S4 scanner.